



# Pore structure, interface properties and photocatalytic efficiency of hydration/dehydration derived TiO<sub>2</sub>/CNT composites

Sandra M. Miranda<sup>a,b</sup>, George Em. Romanos<sup>c,\*\*</sup>, Vlassis Likodimos<sup>c</sup>, Rita R.N. Marques<sup>a</sup>, Evangelos P. Favvas<sup>c</sup>, Fotios K. Katsaros<sup>c</sup>, Konstantinos L. Stefanopoulos<sup>c</sup>, Vítor J.P. Vilar<sup>b</sup>, Joaquim L. Faria<sup>a</sup>, Polycarpos Falaras<sup>c</sup>, Adrián M.T. Silva<sup>a,\*</sup>

<sup>a</sup> LCM – Laboratory of Catalysis and Materials – Associate Laboratory LSRE/LCM, Faculdade de Engenharia, Universidade do Porto, Rua Dr. Roberto Frias s/n, 4200-465 Porto, Portugal

<sup>b</sup> LSRE – Laboratory of Separation and Reaction Engineering, Associate Laboratory LSRE/LCM, Faculdade de Engenharia, Universidade do Porto, Rua Dr. Roberto Frias s/n, 4200-465 Porto, Portugal

<sup>c</sup> Division of Physical Chemistry, Institute of Advanced Materials, Physicochemical Processes, Nanotechnology and Microsystems, NCSR Demokritos, 153 10 Aghia Paraskevi Attikis, Athens, Greece

## ARTICLE INFO

### Article history:

Received 2 May 2013

Received in revised form 28 July 2013

Accepted 7 August 2013

Available online 21 August 2013

### Keywords:

TiO<sub>2</sub>/CNT composites

LN<sub>2</sub> porosimetry

Raman

SAXS

Photocatalysis

## ABSTRACT

Manifold advantages are foreseen by using carbon nanotubes (CNTs) as support for inorganic TiO<sub>2</sub> nanoparticles due to the unique texture/morphology and adsorption capacity of CNTs. Synergistic effects might also result from interfacial charge transfer between the CNTs and TiO<sub>2</sub>. Effective charge transfer has the potentiality to limit electron/hole recombination and shift the TiO<sub>2</sub> photocatalytic response to the visible range. Homogeneous mixing and intimate contact between the graphitic and TiO<sub>2</sub> surfaces are of high importance in order to trigger synergistic effects. Thus, the existence of complementary methods to shed light on both these features is of high importance when developing TiO<sub>2</sub>/CNT composite photocatalysts. In this work, a wide variety of TiO<sub>2</sub>/CNT composites was prepared by a simple hydration/dehydration procedure, using single-wall (SWCNTs) and multi-wall (MWCNTs) carbon nanotubes, either functionalized or not, and TiO<sub>2</sub> nanoparticles of different size. To evaluate the degree of homogeneity between the graphitic and inorganic phases, a new methodology which was based on a complex interpretation of the liquid nitrogen porosimetry (LN<sub>2</sub>) isotherms of the composites and of each phase in the composite separately was developed. Furthermore, interface interaction characteristics were elucidated by micro-Raman spectroscopy while small-angle X-ray scattering (SAXS) measurements provided insight on the surface roughness and micropore structure of the TiO<sub>2</sub>/SWCNT samples. The Raman analysis concluded to the absence of any interfacial interaction. In this context the efficiency of the prepared composites to photocatalytically oxidize caffeine was evaluated in regard to their homogeneity, as derived by the LN<sub>2</sub> method. As expected, in the absence of synergistic effects the photocatalytic efficiency correlated well with the extent of mixing between the CNTs and TiO<sub>2</sub> phases. The discrepancy observed for one of the samples was attributed to the existence of large micropores, a feature that was distinguishable solely by SAXS measurements.

© 2013 Elsevier B.V. All rights reserved.

## 1. Introduction

Recently, much of the research effort focuses on the development of carbon nanotubes (CNTs) mixed with TiO<sub>2</sub> as composite photocatalytic materials to remove organic pollutants from water and air [1–5]. Synergistic effects have already

been observed for the TiO<sub>2</sub>/CNT composites in the degradation of some organic pollutants due to the ability of CNTs to act as electron sink, promoting electron/hole (e<sup>−</sup>/h<sup>+</sup>) separation [6–8].

Up to date, most of the TiO<sub>2</sub>/CNT composites are prepared using methods such as the sol–gel [6,9] or surfactant wrapping sol–gel [10], the solvothermal [8,11], the hydrolysis of titanium tetraisopropoxide in supercritical ethanol [12], the chemical vapour deposition (CVD) [13], the hydration/dehydration [14–16] and the coating via the use of polyethylenimine [17]. Furthermore, techniques such as the introduction of an interface layer of indium tin oxide (ITO) between CNTs and TiO<sub>2</sub> have also been involved

\* Corresponding author. Tel.: +351 225081582; fax: +351 220414908.

\*\* Corresponding author. Tel.: +30 2106503972 3; fax: +30 2106511766.

E-mail addresses: [groman@chem.demokritos.gr](mailto:groman@chem.demokritos.gr) (G.Em. Romanos), [adrian@fe.up.pt](mailto:adrian@fe.up.pt) (A.M.T. Silva).

to minimize the contact resistance of TiO<sub>2</sub>/SWCNT composite films [2].

The application of different synthetic approaches leads to completely different morphologies of the developed TiO<sub>2</sub>/CNT composites that can vary from random physical mixture and TiO<sub>2</sub> covering via chemical bonding, to CNTs wrapping around large TiO<sub>2</sub> nanoparticles. Possible composite's morphologies obtained by the application of the two most common synthesis methods (e.g. the sol–gel and hydrothermal method) have already been postulated [18] and several studies concluded to the point that in general the composite produced with the sol–gel method has more homogeneously dispersed TiO<sub>2</sub> nanoparticles on the surface of CNTs, while the hydrothermal method features compact aggregation of larger TiO<sub>2</sub> nanoparticles loaded on the bundles or networks of CNTs. Such morphologies have also been confirmed via transmission electron microscopy or scanning electron microscopy in many studies using either the sol–gel or the hydrothermal method.

TiO<sub>2</sub>/CNT composites can exhibit photocatalytic activity that strongly depends on the materials morphology. In a recent study [18] it was found that the composite synthesized via the sol–gel method showed higher photocatalytic activity than the composite via hydrothermal method for the oxidation of NO and phenol. This was explained by the individual physicochemical properties of the composite in terms of variation in surface area and crystallite size in a way that affected the e<sup>−</sup>/h<sup>+</sup> recombination efficiency.

Besides the method of preparation, two additional factors were found to influence the photocatalytic performance of the obtained composites, namely the mass ratio CNTs:TiO<sub>2</sub>, and the calcination temperature. Several studies lead to the conclusion that the optimum mass ratio between CNTs and TiO<sub>2</sub> is in the range of 1.5–20% [6,7,18] and argue that the optimum depends also on the target pollutant. The same authors claimed that the extent of heterogeneous covering of TiO<sub>2</sub> could also affect the optimum mass ratio for photocatalytic degradation and this depends significantly on the conditions and synthesis pathway. Apart from this, it is certain that appropriate mass ratios cause the increase of pollutants concentration around TiO<sub>2</sub> and facilitates the photocatalytic degradation of pollutants [19], but an excessive amount of CNTs may reduce the rate of photocatalysis due to elevated scattering of photons [7].

Furthermore, depending on the synthetic procedure (especially for sol–gel), calcination of the composite may be a requirement in order to produce crystalline (anatase, rutile or brookite) titania and stabilize the TiO<sub>2</sub>/CNT composite in an intimate contact. In relevant efforts it was concluded that the presence of TiO<sub>2</sub> lowered significantly the combustion point of MWCNTs [7] and in this regard, inappropriate calcination temperatures led to the gasification of the CNTs in the composites affecting significantly the CNTs:TiO<sub>2</sub> mass ratio. In recent studies [20], much lower photocatalytic performance was reported for TiO<sub>2</sub>/CNT composites that were calcined at temperatures above 350 °C. However, the CNTs synthesis methods (CVD or arc), the type of used CNTs (SWCNTs or MWCNTs) and the CNTs defects and impurities, are additional factors that affect the temperature tolerance to calcination and must be taken into account. It is also necessary to consider the type of the TiO<sub>2</sub> polymorphs, which plays also a very important role in the photocatalytic efficiency of the derived composites. As the bandgap of anatase (3.2 eV) is larger than rutile (3.02 eV), higher redox potential is expected for anatase [21]. Furthermore, anatase also possesses high area density of hydroxyl groups, which can slow the recombination of e<sup>−</sup>/h<sup>+</sup> pairs [22].

In this study TiO<sub>2</sub>/SWCNT and TiO<sub>2</sub>/MWCNT composite photocatalysts with a simple hydration/dehydration method adapted from procedures described in the literature were prepared [14,16]. A SWCNTs:TiO<sub>2</sub> mass ratio of 17% was used and by keeping this important factor constant, functionalized and pristine SWCNTs and TiO<sub>2</sub> photocatalysts of anatase phase and different particle size

were applied. In this framework, it was possible to rationalize the effect of the functionalization of SWCNTs and also the TiO<sub>2</sub> nanoparticle size on the photocatalytic efficiency of the produced composites. Moreover, the effect of MWCNTs:TiO<sub>2</sub> mass ratio on the photocatalytic performance of the produced composites, by using functionalized MWCNTs and one type of TiO<sub>2</sub> that exhibited the larger nanoparticles, was examined. The degradation rate and capacity for caffeine was selected as the indicator of comparison between the photocatalytic efficiency of the several composites, since it was proved in a recently published work [23] that CNTs, namely multi-walled CNTs, when combined with TiO<sub>2</sub> are effective photocatalysts for the degradation of this pollutant.

For the first time the mixing quality of the two phases (CNTs and TiO<sub>2</sub>) in the composites was assessed by a macroscopic method, in the circumstance LN<sub>2</sub> porosimetry. The up to now reports using scanning electron microscopy (SEM) and transmission electron microscopy (TEM) approaches lack significance for the homogeneity of the produced composites at the macroscale, because such a procedure would require a enormous amount of time (and cost) for a meaningful statistical analysis. In addition, Raman spectroscopy was used in the present work as a way to infer about the occurrence, or not, of strong interfacial charge transfer between the two constituent phases. Based on the reported findings, it is plausible that the photocatalytic efficiency could depend solely on the mixing quality of the composites. For making that point, the mixing quality of the composites was correlated to the photocatalytic efficiency over the degradation of caffeine as model compound. Some of the observed deviations to that correlation were explained by the additional effect of adsorption into large micropores (0.8–0.9 nm), which pore structural characterization was obtained by small-angle X-ray scattering (SAXS) measurements.

## 2. Experimental

### 2.1. Carbon nanotubes

In this study, two different CNTs were employed, all synthesized by CVD, namely (i) SWCNTs provided by Cheap Tubes Inc with purity around 90%, a diameter ranging between 1 and 2 nm and length between 0.5 and 2.0 μm (labelled as SNT) and (ii) MWCNTs provided by Nanothinx S.A. with purity around 98.5%, a diameter ranging between 30 and 50 nm and length >10 μm (labelled as MNX). As reference, the best TiO<sub>2</sub>/CNT composite according to our previous work – SA/CNTf-20 [23] – was also prepared, using MWCNTs provided by Shenzhen Nanotechnologies Co. Ltd. with purity ≥ 95%, main range of diameter <10 nm and length of 5–15 μm (labelled hereafter as MNP).

### 2.2. Carbon nanotubes functionalization

0.5 g of CNTs was placed in a 500 mL round bottom flask equipped with a condenser, and 150 mL of HNO<sub>3</sub> with a concentration of 10 mol L<sup>−1</sup> (prepared from 65% HNO<sub>3</sub> – Fluka) was added. The mixture was refluxed under magnetic stirring and heated to boiling temperature for 3 h. Then the solution was allowed to cool until room temperature and the recovered CNTs were washed several times with distilled water up to neutral pH, and then dried at 383 K overnight. This procedure was applied to functionalize all the CNTs, hereafter referred as SNTf, MNXf and MNPf, for functionalized SNT, MNX and MNP, respectively.

### 2.3. Preparation of TiO<sub>2</sub>/CNT composites

Three different types of TiO<sub>2</sub> were used to prepare the TiO<sub>2</sub>/CNT composites, namely two commercial TiO<sub>2</sub> materials – Evonik Degussa TiO<sub>2</sub> (P25) and Sigma Aldrich (SA) – and TiO<sub>2</sub> produced

in our laboratory through a modified acid catalyzed sol–gel method (SG). These bare materials were characterized in our recently published work [23]. The composites were prepared by a simple hydration/dehydration method adapted from procedures described in literature [14–16]. Briefly, 0.1 g of the CNTs were dispersed in ultra-pure water under sonication, TiO<sub>2</sub> was added under stirring, the mixture was heated at 353 K until complete evaporation of water and the resulting composites were dried overnight at 383 K. These composites were prepared with pristine CNTs (labelled as XX/CNT-Y) and functionalized CNTs (XX/CNTf-Y), where “XX” is the type of TiO<sub>2</sub> used (SG, P25 or SA), “CNT” the carbon nanotubes used (SNT, MNX or MNP) and “Y” (5, 10 or 20) corresponds to the mass of CNTs per 100 mass units of bare TiO<sub>2</sub> (i.e. approximately 5, 9 and 17 wt.% of CNTs, respectively).

#### 2.4. Photocatalytic experiments

The degradation of caffeine was studied in a solar simulator (CO.FO.MEGRA model 1500e) equipped with a xenon lamp and a cut-off soda lime glass filter, delivering UV–vis light (500 W,  $\lambda > 350$  nm and irradiance of 43 mW cm<sup>-2</sup> determined with a UV–vis spectroradiometer USB2000+, OceanOptics, USA). In each photocatalytic run, a fixed amount of catalyst (50 mg) was dispersed in 50 mL of a caffeine aqueous solution (50 mg L<sup>-1</sup>) that was continuously bubbled with air. The photocatalytic system and conditions employed were therefore different from those used in our previous work [23]. Prior to irradiation, the suspension was stirred for 30 min under dark conditions, this time being enough to achieve the adsorption–desorption equilibrium of caffeine molecules on the surface of the catalyst. The lamp was turned on (considered as  $t = 0$  for the photocatalytic reaction) and samples were periodically taken and centrifuged for analysis. An experiment in the absence of catalyst was also performed as blank in order to calculate the contribution from direct photolysis. Some experiments were repeated and deviations were never larger than 0.5%.

Samples were analyzed by high performance liquid chromatography (HPLC), using a Hitachi Elite LaChrom instrument equipped with a diode array detector (L-2450), a Purospher Star RP-18 column (250 mm × 4.6 mm, 5  $\mu$ m particles), and a solvent delivery pump (L-2130) at a fixed flow rate of 1 mL min<sup>-1</sup>. At first, the column was equilibrated with a A:B (70:30) mixture of ultra-pure water (A) and methanol (B), followed by a linear gradient run to A:B (37:63) in 20 min. Caffeine concentration was determined at the maximum absorption wavelength (274 nm) on the chromatograms taken using the EZChrom Elite chromatography data handling software (Version 3.1.7). This absorbance was found to be linear over the whole considered range (a maximum relative standard deviation of 2%).

#### 2.5. Analytical Instruments

LN<sub>2</sub> (77 K) porosimetry experiments were performed with the Autosorb-1-MP nitrogen porosimeter (Quantachrome) equipped with krypton upgrade. Before the measurement all samples were outgassed at 200 °C under high vacuum for 24 h on the outgassing stations of the instrument (6% range of variability).

Micro-Raman spectra were measured in backscattering configuration on a Renishaw inVia Reflex system using an Ar<sup>+</sup> ion laser ( $\lambda = 514.5$  nm) and a high power near infrared (NIR) diode laser ( $\lambda = 785$  nm) as excitation sources. The laser power density was kept at low levels (<0.03 mW/ $\mu$ m<sup>2</sup>) to avoid local heating of the samples. A large number of spectra were acquired from different spots for each studied sample, while the frequency shifts were calibrated by an internal Si reference. Spectral deconvolution was carried out by non-linear least square fitting of the Raman peaks by Lorentzian lineshapes.

**Table 1**

Pore structure characteristics of a control sample consisting of two separated SWCNTs (SNTf) and TiO<sub>2</sub> (SA) phases.

	Mixed sample	Predicted	Deviation % <sup>a</sup>
$S_{\text{BET}}$ (m <sup>2</sup> g <sup>-1</sup> )	82.1	84.7	−3.17
Total pore volume – V (mL g <sup>-1</sup> )	0.309	0.321	−3.9
Micropore volume at $P/P_0 = 0.1$ (mL g <sup>-1</sup> )	0.0308	0.0315	−2.27
Average pore radius $2 \times (V/S)$ (nm)	7.5	7.6	−1.3
Ultra-micropore volume at $P/P_0 = 0.0001$ (mL g <sup>-1</sup> )	0.0104	0.0094	+9.6

<sup>a</sup> On the basis of the predicted.

A Jeol JSM 7401F Field Emission Scanning Electron Microscope equipped with Gentle Beam mode and the new r-filter was employed to characterize the morphology of the developed TiO<sub>2</sub>/CNT materials. Gentle Beam technology can reduce charging and improve resolution, signal-to-noise, and beam brightness, especially at low beam voltages (down to 100 V).

The SAXS measurements were carried out at 293 K using a Rigaku system (SMAX-300) provided by JJ X-Ray Systems, connected to a sealed tube CuK $\alpha$  X-ray generator. Silver behenate has been used as a standard SAXS calibrant for evaluating the scattering vector,  $Q$  from the sample-to-detector distance ( $Q = 4\pi \sin \theta / \lambda$ , where  $\lambda$  and  $2\theta$  are the wavelength and the scattering angle respectively). The  $Q$  range varied approximately between 0.04 to 0.3 nm<sup>-1</sup>.

### 3. Results and discussion

#### 3.1. LN<sub>2</sub> porosimetry results of TiO<sub>2</sub>/SWCNT

LN<sub>2</sub> (77 K) porosimetry experiments were carried out on all the CNTs and TiO<sub>2</sub> precursor materials as well as on their mixtures prepared with the hydration/dehydration method. The following equation was applied to interpret the nitrogen gas uptake results at each relative pressure ( $P/P_0$ ):

$$\left(\frac{V_{\text{ads}}}{g}\right)_{\text{mixt}} = \left(\frac{V_{\text{ads}}}{g}\right)_{\text{CNT}} y + \left(\frac{V_{\text{ads}}}{g}\right)_{\text{TiO}_2} (1 - y) \quad (1)$$

where  $(V_{\text{ads}}/g)_{\text{CNT}}$  is the gas uptake capacity (standard gas volume) of 1 g of the CNTs  $(V_{\text{ads}}/g)_{\text{TiO}_2}$  is the relevant gas uptake capacity of TiO<sub>2</sub> and  $y$  is the mass fraction of the CNTs in the mixed sample. The purpose was to derive a predicted LN<sub>2</sub> isotherm  $((V_{\text{ads}}/g)_{\text{mixt}}$  vs  $P/P_0$ ) corresponding to an “imaginary”, not well mixed sample, consisting of SWCNTs or MWNTs and TiO<sub>2</sub> material, at a mass ratio identical to that applied in the hydration/dehydration procedure. The accuracy of the proposed methodology was examined as follows. A small diameter (6 mm) glass cell of the nitrogen porosimeter was filled with specific amounts of the functionalized SWCNTs and the SA sample (17.3 and 67.3 mg respectively), the one on the top of the other, without any pre-mixing between them. The experimentally obtained LN<sub>2</sub> isotherm of this “control” sample is presented in Fig. 1 in comparison with the predicted one derived by applying the above Eq. (1) and a mass fraction of (17.3/84.6) for the SWCNTs.

The values of the BET surface area ( $S_{\text{BET}}$ ) and other important pore structure characteristics extracted from these two isotherms are presented in Table 1, together with their deviation.

It can be seen that with the exception of the ultra-micropore volume ( $P/P_0 < 0.0001$ ), all the other experimentally obtained parameters deviate slightly (negatively) from the predicted values. These deviations do not exceed the threshold of 4% and can be attributed to the inaccuracy of sample weighting and most important, to the different mass loss of each material (SNTf, SA) during the outgassing. It should be noted that the outgassing of the mixed (control) sample took place in two steps, e.g. the functionalized

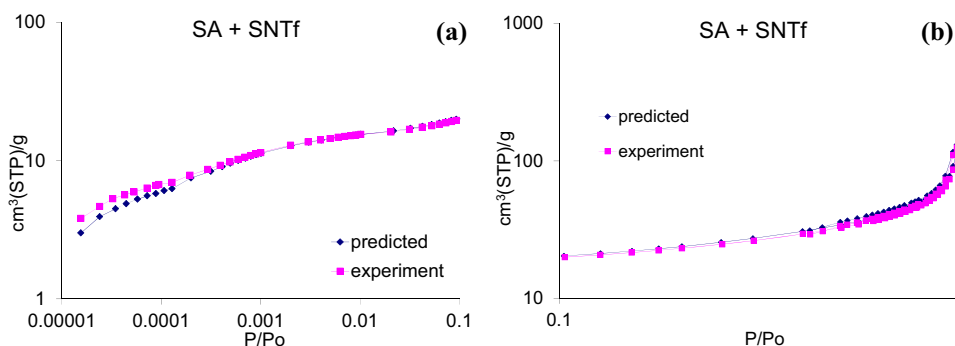


**Fig. 1.** Comparison between the experimental and predicted isotherm of the control sample (i.e. without any pre-mixing). (a) Micropore region of relative pressures, (b) Mesopore region.

SNTf were first outgassed and weighted and subsequently the TiO<sub>2</sub> sample (SA) was introduced into the measurement cell and the mixture outgassed again and weighted. However the contact of the outgassed SNTf with the atmospheric air during the introduction of the SA into the glass cell could not be avoided. Important to note is that the higher deviation (−3.9%) was observed between the predicted and measured value of the total pore volume as a consequence of the inaccuracy of the pressure measurement at relative pressures  $P/P_o$  above 0.99. Examining the two isotherms at the ultra-micropore region ( $P/P_o < 0.0001$ ) it can be seen that, opposite to the other pore structure characteristics, the deviation was in favour of the real mixed sample.

The ultra-micropore ( $P/P_o < 0.0001$ ) and micropore ( $0.0001 < P/P_o < 0.1$ ) pressure area of the LN<sub>2</sub> isotherm can provide important information on the density of SWCNTs aggregation into the formed bundles and on the accessibility of the gas (N<sub>2</sub>) molecules into the interstitial and bore space of the single-wall nanotubes.

Microporosity, characterizes solely the SWCNTs and not the TiO<sub>2</sub> phase. Thus, it is reasonable to expect significant alteration of the micropore volume between the predicted isotherm and the real one upon efficient mixing of the two different materials; i.e. the TiO<sub>2</sub> nanoparticles could prohibit the access of gas into the bore of the nanotubes or distort their dense aggregation or expand the distance between the nanotube bundles. Conclusively, efficient mixing between the SWCNTs and the TiO<sub>2</sub> must lead to a decline of the micropore and ultra-micropore volume and a shift of the size distribution of the pores towards larger values. In this regard, higher negative deviations on the values of these parameters in comparison to those derived from the predicted isotherms indicate better mixing and increase the possibility for larger contact areas between the TiO<sub>2</sub> and SWCNTs phases. Moreover, the smaller size of the TiO<sub>2</sub> nanoparticles can be beneficial for their incorporation in between the SWCNTs bundles, while SWCNTs functionalization was initially expected to lead to enhanced interfacing between the two materials since hydrophilic nanotubes could be easier dispersed and untangled in the water solution.

Before proceeding with the discussion on the obtained results and the elucidation of the effects of the TiO<sub>2</sub> particle size and SWCNTs functionalization on the mixing quality, we had to investigate if the volume ratio of the SWCNTs to the TiO<sub>2</sub> in the composites correlates with the deviations obtained for any of the pore structural characteristics. Thus the bulk density ( $\rho_{\text{bulk}}$ ) of each precursor material was calculated from its total pore volume and solid density (4.23 cm<sup>3</sup> g<sup>−1</sup>, TiO<sub>2</sub> and 1.85 cm<sup>3</sup> g<sup>−1</sup>, SWCNTs) and was further applied to extract the volume ratio using the following equation:

$$V_{\text{ratio}} = \frac{(1/\rho_{\text{bulk}})_{\text{SWCNTs}} \times y}{(1/\rho_{\text{bulk}})_{\text{TiO}_2} \times (1 - y)} \quad (2)$$

where  $y$  is the mass fraction of the SWCNTs in the respective mixed sample.

The LN<sub>2</sub> isotherms obtained for all the mixed samples prepared with the functionalized (XX/SNTf-20) or pristine SWCNTs (XX/SNT-20) in comparison to the predicted ones are presented in Fig. 2.

The derived SWCNTs/TiO<sub>2</sub> volume ratios are included in Table 2, together with the values of the extracted from the isotherms pore structure characteristics and the deviation between the real and predicted experiments. Examining the relevant plots, no correlation was concluded between the SWCNTs/TiO<sub>2</sub> volume ratio and the obtained deviations (the plots were constructed with the data of Table 2, but not included in the manuscript). Although someone could expect better mixing for the 1:1 SWCNTs/TiO<sub>2</sub> volume ratio this was not proved for the prepared composites.

As a general rule, the micropore and ultra-micropore volume calculated from the experimentally obtained isotherms (Fig. 2, Table 2) was lower than the predicted one with only exception for the hybrids produced with the SG sample. Surprising is the fact that the functionalization of the SWCNTs has not any effect on the mixing extent with the SA nanoparticles (microporosity deviations are identical, see Table 2) and even more surprising that the best mixing (larger ultra-micropore volume deviation) was achieved for the P25 nanoparticles with the non-functionalized SWCNTs, while the sample prepared with hydration/dehydration between P25 and functionalized SWCNTs was identical to a “control” sample (no deviations from the predicted). Based on the above, it is possible to state that the functionalization of the SWCNTs generates self-standing bundles where the nanotubes remain tangled through stronger van der Waals forces. Probably the bundles are better dispersed in the water solution during hydration but the nanotubes in each bundle are not disentangled.

On the other hand the smaller P25 nanoparticles of 20 nm size, compared to the SA ones (50–100 nm) can be easily incorporated into the inter-nanotube space of a partially loosened bundle during the hydration of the non-functionalized SWCNTs and distort the ultra-micropore structure ( $P/P_o < 0.0001$ ) generated by their interstitial space. Thus we can state that in the case of the SA-TiO<sub>2</sub>, the micropore volume decline (deviation) is uniform over the entire micropore size area (Fig. 2a and c), as a consequence of the large TiO<sub>2</sub> nanoparticles that partially block the entrance of N<sub>2</sub> molecules into the bore space of the nanotubes that constitute the bundle. On the other hand in the case of P25, the smaller TiO<sub>2</sub> nanoparticles are also incorporated into the ultra-microporous/inter-nanotube space of a bundle and for this reason (Fig. 2g), the pore volume deviation in the ultra-micropore area is much more intense.

In regard to the hybrid samples prepared with the use of the sol-gel derived TiO<sub>2</sub> (SG), it is once again concluded that better mixing occurred with the non-functionalized SWCNTs. The very small SG nanoparticles (SG nanoparticles were significantly smaller



than commercial P25 and SA) could be easily incorporated in between the nanotubes of a disentangling SWCNTs bundle during hydration and for this reason we can observe a negative ultra-micropore volume deviation (Fig. 2I, Table 2). What is completely different in the case of SG is that the micropore and mesopore volume deviated positively from the predicted values. Thus, the SG nanoparticles that are not interposed into the SWCNTs bundles tend to aggregate forming larger plate-like particles (see also SEM Fig. 6) that generate an additional meso-macropore structure defined by the space between them. Incorporation of the untangled bundles of the SWCNTs in between these plates leads to the enhancement of mesoporosity, e.g. macropores are transformed to mesopores.

### 3.2. $LN_2$ porosimetry results of $TiO_2$ /MWCNT

MWCNTs, due to their large size and loose arrangement, can be better mixed with the  $TiO_2$  nanoparticles. Parameters such as the  $TiO_2$  nanoparticle size and the degree of graphitic surface functionalization are not expected to affect the morphology of the respective  $TiO_2$ /CNT composites. In this work, MWCNTs have been solely investigated in relation to the effect of their content on the pore structure characteristics of the prepared

hybrids. Therefore, the mixed samples were prepared with different mass ratio between the functionalized MWCNTs (MNxf) and the SA material. According to the specifications provided by the manufacturer of the MWCNTs (diameter 30–50 nm, number of layers 25–50) we could estimate an average nanotube bore diameter of 15 nm. The average pore dimension obtained from the  $LN_2$  isotherm was 27 nm due to the existence of larger pores formed between the nanotube bundles. Thus, mesopores smaller than 15 nm in the specific functionalized MWCNTs sample correspond solely to the interstitial space between the nanotubes constituting a bundle. On the other hand the average pore size of the SA powder calculated from the respective  $LN_2$  isotherm was 94 nm, indicating the existence of larger pores (>100 nm) that could accommodate carbon nanotube bundles of small size. In this context we can distinguish between two different ways of mixing and the respective effects. Intercalation of the MWCNTs bundles in the  $TiO_2$  inter-particle space will cause the enhancement of mesoporosity for relative pressures  $P/P_0 > 0.8$ . Furthermore, interposing of the  $TiO_2$  nanoparticles in between the individual MWCNTs will have a strong effect on the deviation between the predicted and real  $LN_2$  isotherms in the small pressures region and the mesopore region ( $P/P_0$  up to 0.1 and to 0.8 respectively).

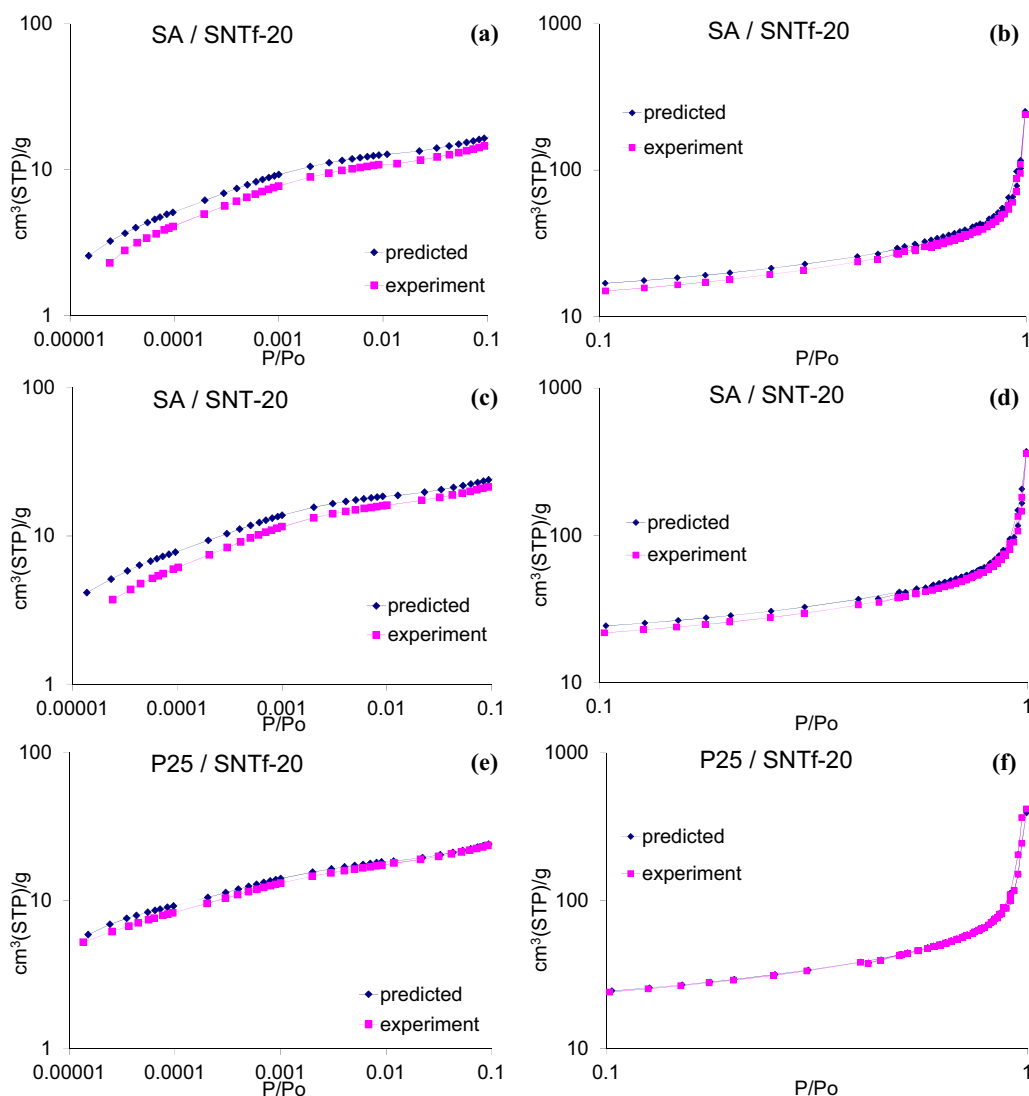


**Fig. 2.** The experimentally obtained and predicted isotherms for the samples prepared with the use of SWCNTs. On the left column are shown the micropore and on the right column the mesopore pressures area of the isotherms.

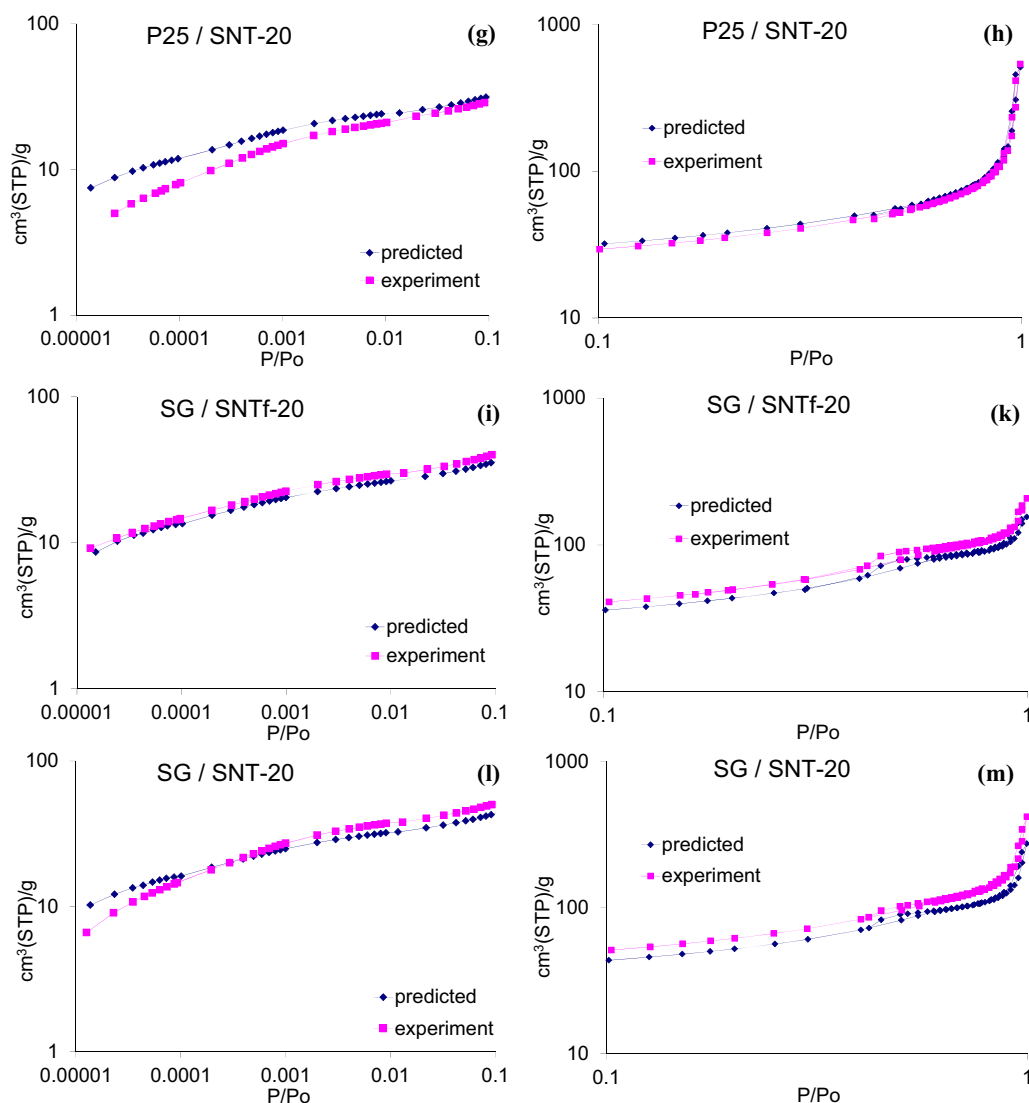


Fig. 2. (Continued).

What can be clearly observed in the isotherm plots presented in Fig. 3 is that the different MWCNTs content resulted to quite different pore structure characteristics of the prepared hybrids. However, no correlation was concluded between the volume ratio MWCNTs:TiO<sub>2</sub> (Table 3) and the deviations from the predicted isotherm, as was also the case with the SWCNTs.

More specific the SA/MNXf-5 sample presented a large negative deviation between the experimentally derived pore volume (up to relative pressures  $P/P_0 = 0.1$ ) and the predicted one and no deviation of the mesopore volume for relative pressures up to 0.8. Moreover the total mesopore volume was 10% higher than expected. These facts indicate that during the hydration/dehydration procedure the larger of the bundles, consisting of a high number of MWCNTs, have intercalated TiO<sub>2</sub> nanoparticles into their inter-nanotube space, whereas the smaller of the bundles were interposed in the interstitial space of a fraction of the TiO<sub>2</sub> nanoparticles generating an extra mesopore volume.

The SA/MNXf-10 sample presented significant deviations from the predicted isotherm only in the low pressures area ( $0.0001 < P/P_0 < 0.1$ ) and the small mesopore region ( $0.3 < P/P_0 < 0.8$ ). Probably the arrangement of the carbon nanotubes and the TiO<sub>2</sub> nanoparticles after the hydration/dehydration was similar to what happened with the SA/MNXf-5 sample but

due to the larger content of the MWCNTs, the disentanglement of a small portion of them was not distinguishable by the LN<sub>2</sub> porosimetry and as a consequence the pore volume at very low relative pressures remained unaffected. What is different from the SA/MNXf-5 sample is that the total mesopore volume is 12.6% lower than expected. This indicates that the bundles were not intercalated in between the TiO<sub>2</sub> nanoparticles probably due to their large size; i.e. the higher MWCNTs content leads to the formation of bundles consisting of a higher number of MWCNTs.

When the percentage of the MWCNTs in the hybrids was higher, SA/MNXf-20, it was obtained the higher deviation in the low pressures area and the small mesopore region and no deviation in the total mesopore volume, again due to the formation of large diameter MWCNTs bundles. What is important to note for this sample is that the deviation between the real and predicted isotherm is uniform in all the relative pressures area, indicating that in this sample we achieved the most uniform mixing between the two phases. We can attribute this to the volume fraction between the two phases which was close to one but we should once again state that there was not any correlation of the MWCNTs percentage with the obtained deviations between the experimentally derived and predicted pore structure characteristics.

**Table 2**

Pore structure characteristics derived from the real experiments and the predicted (Pred.) isotherms of the TiO<sub>2</sub>/SWCNT hybrids. Included is the deviation (Dev. %) between them.

	SA/SNTF-20	Pred.	Dev. %	SA/SNT-20	Pred.	Dev. %
Volume ratio (SWCNTs:TiO <sub>2</sub> )	0.63	–	–	1.05	–	–
S <sub>BET</sub> (m <sup>2</sup> g <sup>−1</sup> )	65.3	70.8	−8.4	92.8	101.5	−9.4
Total pore volume – V (mL g <sup>−1</sup> )	0.37	0.39	−5.4	0.56	0.574	−2.5
Micropore volume at P/P <sub>0</sub> = 0.1 (mL g <sup>−1</sup> )	0.023	0.026	−13	0.0338	0.038	−12.4
Average pore radius 2 × (V/S) (nm)	11.4	11	+3.5	12	11.3	+5.8
Ultra-micropore volume at P/P <sub>0</sub> = 0.0001 (mL g <sup>−1</sup> )	0.0063	0.0075	−19	0.0095	0.0114	−20
	P25/SNTF-20	Pred.	Dev. %	P25/SNT-20	Pred.	Dev. %
Volume ratio (SWCNTs:TiO <sub>2</sub> )	0.42	–	–	0.7	–	–
S <sub>BET</sub> (m <sup>2</sup> g <sup>−1</sup> )	105.6	106.4	−0.76	128.1	137.2	−7.1
Total pore volume – V (mL g <sup>−1</sup> )	0.645	0.608	+5.7	0.832	0.79	+5.04
Micropore volume at P/P <sub>0</sub> = 0.1 (mL g <sup>−1</sup> )	0.0372	0.038	−2.15	0.045	0.0496	−10.2
Average pore radius 2 × (V/S) (nm)	12.2	11.4	+6.55	13	11.54	+11.2
Ultra-micropore volume at P/P <sub>0</sub> = 0.0001 (mL g <sup>−1</sup> )	0.0128	0.0143	−11.7	0.012	0.018	−50
	SG/SNTF-20	Pred.	Dev. %	SG/SNT-20	Pred.	Dev. %
Volume ratio (SWCNTs:TiO <sub>2</sub> )	0.95	–	–	1.59	–	–
S <sub>BET</sub> (m <sup>2</sup> g <sup>−1</sup> )	184.9	159.5	+13.7	226.6	190.4	+16
Total pore volume – V (mL g <sup>−1</sup> )	0.32	0.24	+25	0.65	0.424	+34.8
Micropore volume at P/P <sub>0</sub> = 0.1 (mL g <sup>−1</sup> )	0.0634	0.0558	+12	0.079	0.0675	+14.5
Average pore radius 2 × (V/S) (nm)	3.48	3	+13.8	5.7	4.5	+21
Ultra-micropore volume at P/P <sub>0</sub> = 0.0001 (mL g <sup>−1</sup> )	0.0226	0.0208	+7.9	0.0225	0.025	−11

### 3.3. SEM analysis

The SEM analysis of the prepared hybrids revealed a nanostructured morphology which is in accordance to the findings of the LN<sub>2</sub> methodology described in Sections 3.1 and 3.2.

Focusing on the two samples prepared with P25, it is possible to see that in the case of the functionalized SWCNTs (Fig. 4a, c and e) there are two well-separated phases, e.g. bundles of carbon nanotubes and TiO<sub>2</sub> nanoparticles aggregates, with no sign of mixing in between them. This is exactly the image we could devise from the interpretation of the LN<sub>2</sub> porosimetry results (Fig. 2e and f) where the deviation between the predicted and experimental isotherm was minor. Even in the image obtained at the higher magnification (Fig. 4e), some isolated SWCNTs bundles with size of 20–35 nm seem to lay on the external surface of the TiO<sub>2</sub> nanoparticle aggregates. Contrary to that, the SEM images obtained for the hybrid prepared with the pristine SWCNTs showed interposing of TiO<sub>2</sub> nanoparticles inside the SWCNTs bundles (marked areas in Fig. 4b and d) while in Fig. 4f carbon nanotube bundles coming out from the TiO<sub>2</sub> aggregates can be distinguished. This sample is the one that exhibited the highest deviation between the experimental and predicted isotherm at the ultra-micropore region of pressures (Fig. 2g).

Concerning the SA-based hybrids, the SEM images revealed the similarity of the mixing quality between those prepared with the use of pristine and functionalized SWCNTs respectively. The similar morphologies observed in the SEM micrographs agree with the conclusions of the LN<sub>2</sub> methodology where the deviations between the experimental and predicted isotherms were almost identical for the two different samples (Fig. 2a–d). In a general view

the mixing between the two phases in both samples seems poor, mainly because of the large size of the TiO<sub>2</sub> nanoparticles. Areas with a higher mixing degree are marked in Fig. 5b and c. It can be seen that there are smaller size TiO<sub>2</sub> aggregates dispersed on the surface or in the SWCNTs bundles. However this is far from what it is observed in the sample prepared with P25 and pristine SWCNTs.

SEM micrographs of the hybrids prepared with SG and functionalized SWCNTs are presented in Fig. 6. Larger and smaller plate-like particles, formed by the aggregation of very small TiO<sub>2</sub> nanocrystallites are distinguishable in all the presented micrographs. Large bundles of SWCNTs are also distinguishable which are intercalated in between the plate like particles generating an extra mesopore volume as already devised by the interpretation of the LN<sub>2</sub> adsorption isotherms.

In Fig. 7a–c, the morphological characteristics of the SA/MNXf-5 sample evidence the existence of isolated MWCNTs dispersed around the large TiO<sub>2</sub> nanoparticles while the co-existence of small MWCNTs bundles interposed between the aggregates of TiO<sub>2</sub> nanoparticles is also confirmed (Fig. 7b and c). The sample with the 10% MWCNTs content (SA/MNXf-10), exhibits also extended areas where MWCNTs are effectively dispersed (Fig. 7d) but due to their higher content, MWCNTs are preferably organized in bundles of larger size that cannot be intercalated into the inter-particle space of the TiO<sub>2</sub> aggregates (Fig. 7e and f). The sample prepared with the higher content of MWCNTs (SA/MNXf-20) exhibits all the aforementioned characteristics; e.g. untangled MWCNTs, bundles of small size interposed between TiO<sub>2</sub> nanoparticles and bundles of large size, in a well-balanced distribution within the sample. This homogeneity is mainly proclaimed in Fig. 7h, where all these characteristics can be distinguished in a very small area of the sample. In

**Table 3**

Pore structure characteristics derived from the real experiments and the predicted (Pred.) isotherms of the TiO<sub>2</sub>/MWCNT hybrids. Included is the deviation (Dev. %) between them.

	SA/MNXf-5	Pred.	Dev. %	SA/MNXf-10	Pred.	Dev. %	SA/MNXf-20	Pred.	Dev. %
Volume ratio (MWCNTs:TiO <sub>2</sub> )	0.19	–	–	0.38	–	–	0.77	–	–
S <sub>BET</sub> (m <sup>2</sup> g <sup>−1</sup> )	18.6	20.5	−10.2	22.5	28	−24.4	30.9	41.4	−10.5
Total pore volume – V (mL g <sup>−1</sup> )	0.374	0.336	+10.1	0.33	0.378	−12.6	0.438	0.452	−3.2
Pore volume up to P/P <sub>0</sub> = 0.1 (mL g <sup>−1</sup> )	0.00494	0.00656	−32.8	0.00704	0.00914	−30	0.0096	0.0136	−41.6
Average pore radius 2 × (V/S) (nm)	40.3	32.7	+18.9	29.38	27	+8.1	28.4	21.9	+22.8
Pore volume up to P/P <sub>0</sub> = 0.0001 (mL g <sup>−1</sup> )	0.00133	0.00186	−47.3	0.0021	0.00235	−11.9	0.0024	0.0032	−33.3

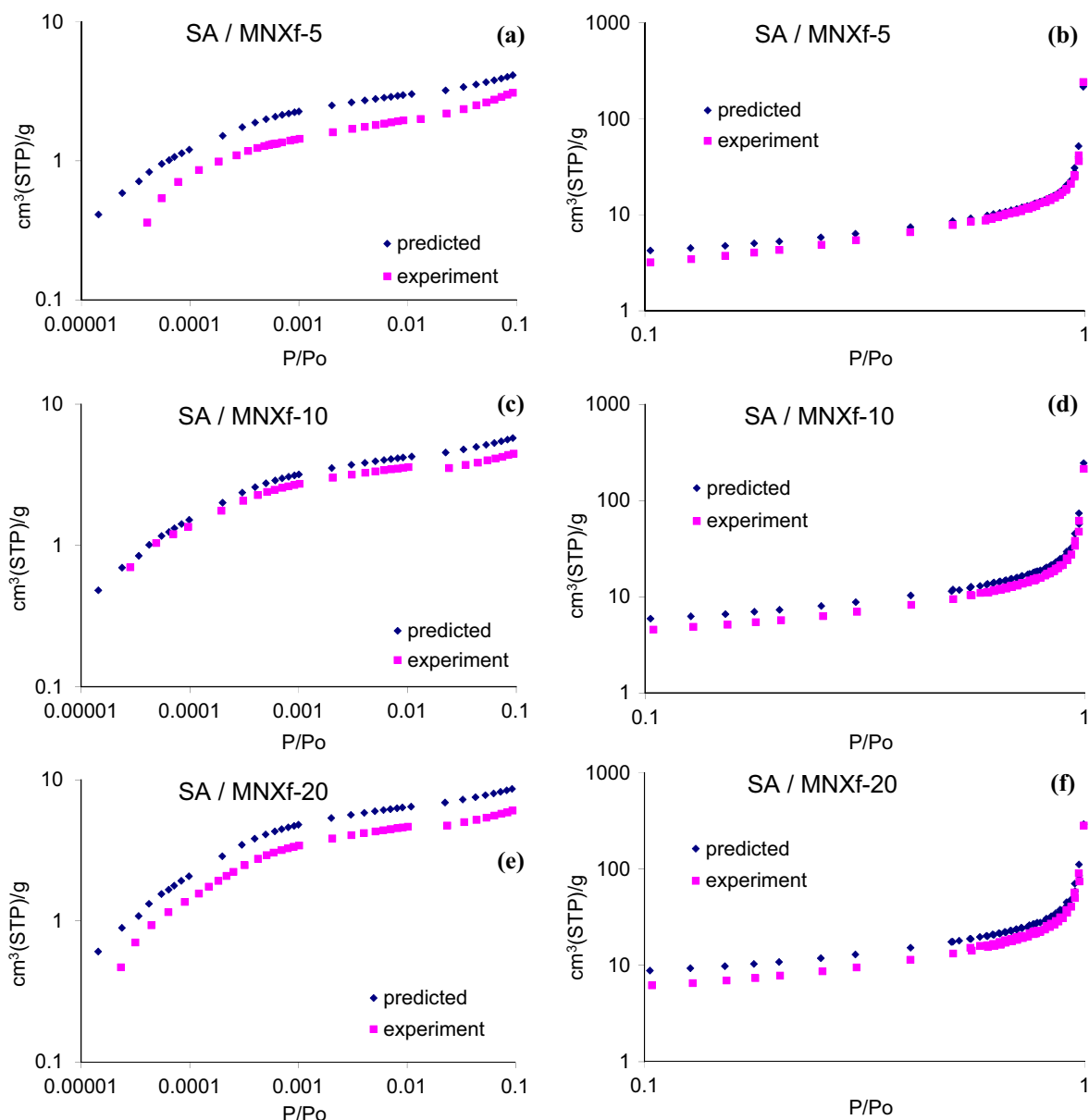


**Fig. 3.** The experimentally obtained and predicted isotherms for the samples prepared with the use of functionalized MWCNTs and SA TiO<sub>2</sub>. On the left column are shown the micropore and on the right column the mesopore pressures area of the isotherms.

general, the findings of the SEM analysis were in good accordance with the conclusions derived from the new methodology proposed in this work for the interpretation of the LN<sub>2</sub> porosimetry results.

From the up to now analysis (LN<sub>2</sub> porosimetry and SEM), important conclusions regarding the effect of several parameters to the mixing quality of hybrid materials that are prepared with the application of a simple hydration/dehydration procedure making use of SWCNTs or MWCNTs and TiO<sub>2</sub> nanoparticles were extracted. The more significant and unexpected result is that the decoration of the graphitic surface with oxygen bearing functionalities has negligible effect on the extent of mixing between the two phases, in particular for P25- and SG-based TiO<sub>2</sub>/SWCNT composites.

Smaller TiO<sub>2</sub> nanoparticles are easily intercalated in the interstitial space of the nanotubes as expected whereas the volume ratio between the carbon nanotubes and the TiO<sub>2</sub> was not a significant parameter and no correlation was concluded between the volume ratio and the mixing extent. Finally completely different pore structure characteristics were observed for the samples

prepared with SG compared to those prepared with the commercial TiO<sub>2</sub> nanoparticles. The large plate-like SG particles do not affect the micropore and ultramicropore volume of the SWCNTs bundles. Contrary they host in their interstitial space large bundles of SWCNTs, a morphology that caused a positive deviation of all the examined pore structure characteristics compared to the predicted ones. Considering that the decrease of the carbon nanotube microporosity, i.e. disentanglement of the carbon nanotube bundles or plugging of the carbon nanotube bore space could be a measure on how much efficient is the mixing of TiO<sub>2</sub> with the graphitic phase, it is possible to rank the produced hybrids as following. For the case of SWCNTs: P25/SNT-20 ≫ SA/SNT-20 ≈ SA/SNTf-20 ≫ P25/SNTf-20 ≈ SG/SNT-20 > SG/SNTf-20. For the case of MWCNTs: SA/MNXf-5 > SA/MNXf-20 > SA/MNXf-10. However a question has still to be answered. Is the mixing extent enough to predict the photocatalytic efficiency of the produced hybrids? Normally, efficient mixing enhances the probability for achieving the maximum possible interfacing between the graphitic and TiO<sub>2</sub>



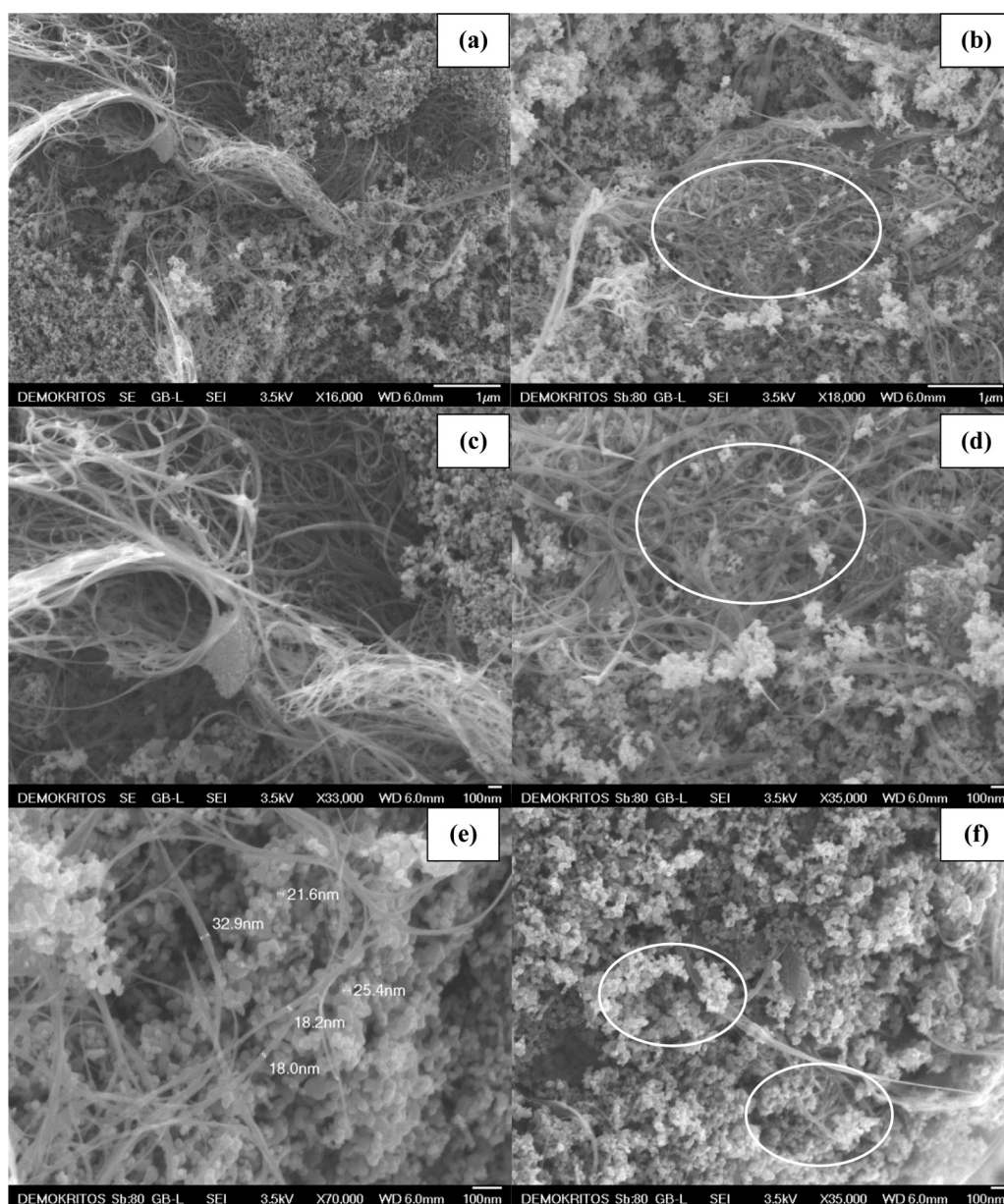


Fig. 4. SEM images of the hybrids prepared with P25 and (a, c, e) functionalized or (b, d, f) non-functionalized SWCNTs (P25/SNTf-20 or P25/SNT-20, respectively).

phase. To answer this question extensive Raman analysis of all the composites prepared in this work was performed.

### 3.4. Resonance Raman spectroscopy on $\text{TiO}_2$ /SWCNT

Fig. 8 summarizes the Raman spectra of the XX/SNT-20 and XX/SNTf-20 composites in comparison with those of their individual constituents at two excitation wavelengths in the NIR (785 nm) and visible range (514.5 nm). The characteristic Raman-active modes of the anatase  $\text{TiO}_2$  phase were readily detected at 142 ( $E_{g(1)}$ ), 196 ( $E_{g(2)}$ ), 395 ( $B_{1g(1)}$ ), 516 (superposition of  $A_{1g}$  and  $B_{1g(2)}$ ) and 638  $\text{cm}^{-1}$  ( $E_{g(3)}$ ) for the SA/SNT-20 and SA/SNTf-20 composites at both NIR and visible excitations, as shown in Fig. 8a and b. These frequencies are close to those expected for bulk anatase due to the relatively large size of the SA nanoparticles ( $\sim 100$  nm), which precludes significant effects due to optical phonon confinement that leads to the broadening and shift of the Raman bands in nanosized  $\text{TiO}_2$  [24].

On the other hand, only the most intense anatase  $E_{g(1)}$  mode could be traced for the P25/SNT-20 and P25/SNTf-20 composites at 785 nm, as depicted in the inset of Fig. 8c, reflecting the appreciably reduced Raman scattering efficiency of P25  $\text{TiO}_2$  nanoparticles ( $\sim 20$  nm) compared to the much larger SA nanoparticles ( $\sim 100$  nm). The  $\text{TiO}_2$  Raman modes of P25, comprising the anatase vibrational modes together with a weak contribution from the minor rutile phase [25], were fully resolved at 514.5 nm. SWCNTs were likewise identified in the composite materials by their characteristic Raman modes, the most prominent being the first-order ones including the low frequency radial breathing modes (RBM) ( $< 300 \text{ cm}^{-1}$ ) and the tangential G modes ( $\sim 1590 \text{ cm}^{-1}$ ) as well as the highly dispersive defect-induced D band and its overtone at 2D ( $G'$  band), arising from one-phonon and two phonon double resonant processes, respectively [26]. The Raman intensity of the anatase modes was markedly enhanced relative to those of the SWCNTs at 514.5 nm, indicating a different dependence of the Raman cross section on the excitation laser energy for  $\text{TiO}_2$  and SWCNTs. This effect and the size dependence of the Raman

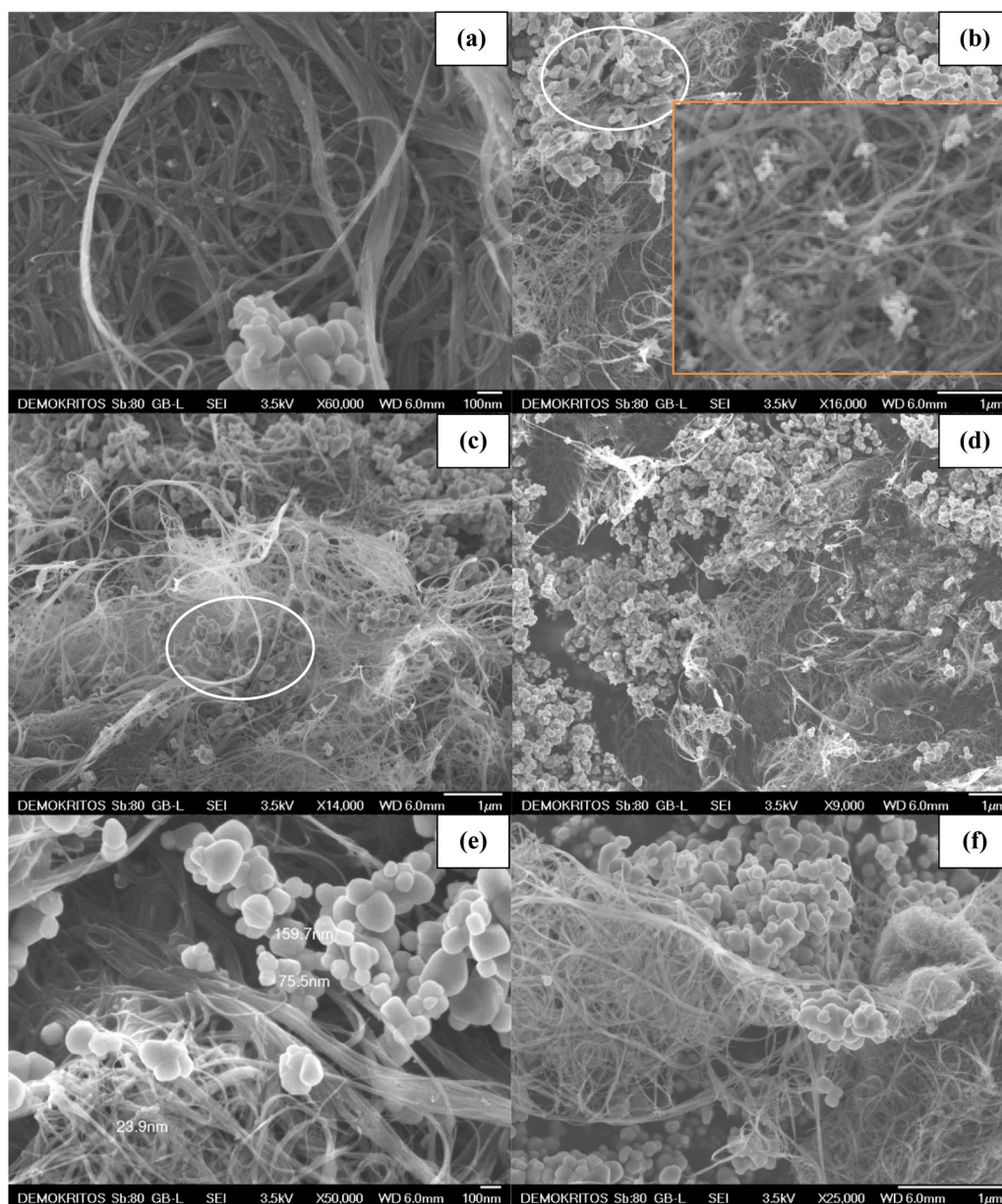


**Fig. 5.** SEM images of the hybrids prepared with SA and (a, c, e) functionalized or (b, d, f) non-functionalized SWCNTs, SA/SNTf-20 or SA/SNT-20, respectively.

scattering efficiency of the  $\text{TiO}_2$  nanoparticles together with the variable loading of the two components can rationalize the large diversity of the CNT/ $\text{TiO}_2$  relative intensities that have been reported for their composite Raman spectra in the literature [27–33].

Comparative analysis of the XX/SNT-20 and XX/SNTf-20 Raman spectra with those of the SNT and SNTf by fitting the tangential doublet ( $G^-$  and  $G^+$ ) modes and the defect-induced  $D$  band in the range of  $1200\text{--}1700\text{ cm}^{-1}$ , has shown minor frequency shifts at both 514.5 and 785 nm. However, the intensity ratio  $I_D/I_G$  derived from the integrated areas of the  $D$  and  $G$  bands ( $I_G = I_{G^-} + I_{G^+}$ ), which is the characteristic probe of defects on the surface of SWCNTs [34,35], increased appreciably for both SA and P25/SNTf-20 composites compared to the SNT and SNTf (Fig. 8). This increase, which follows the excitation laser dependence of the  $I_D/I_G$  ratio in nanographites [34] and oxidized SWCNTs [35], suggests that wet mixing of both types of  $\text{TiO}_2$  nanoparticles with SWCNTs has an effect similar to the formation of defects on the carbon nanotube structure.

Furthermore, the presence of strong coupling and electron transfer at the  $\text{TiO}_2$ /SWCNT interface leading to electron/hole doping of the SWCNTs would be sensitively reflected in their Raman spectra through the attenuation of the SWCNT resonance Raman scattering [36]. However, the relative RBM intensity was hardly affected for the composites with the pristine SWCNTs, especially for P25/SNT-20, as shown in the insets of Fig. 8a and c. Furthermore, instead of attenuation, enhancement of the RBM intensity was observed for both the SA/SNTf-20 and P25/SNTf-20 composites relatively to the SNTf, recovering the RBM intensity of the pristine SWCNTs. A rather weak enhancement was also observed for the second order  $G'$  band intensity in the case of the SA/SNTf-20 and P25/SNTf-20 compared to SNTf, as shown in the rights insets of Fig. 8a–d. The absence of any appreciable shifts of the SWCNTs Raman bands upon mixing with the  $\text{TiO}_2$  nanoparticles shows that the  $\text{TiO}_2$ –SWCNT interaction in the composites prepared by the hydration/dehydration method does not involve any strong interfacial interaction. The presence of weak electronic coupling was further supported by a slight ( $\sim 1\text{ cm}^{-1}$ ) upshift of the  $E_{g(1)}$



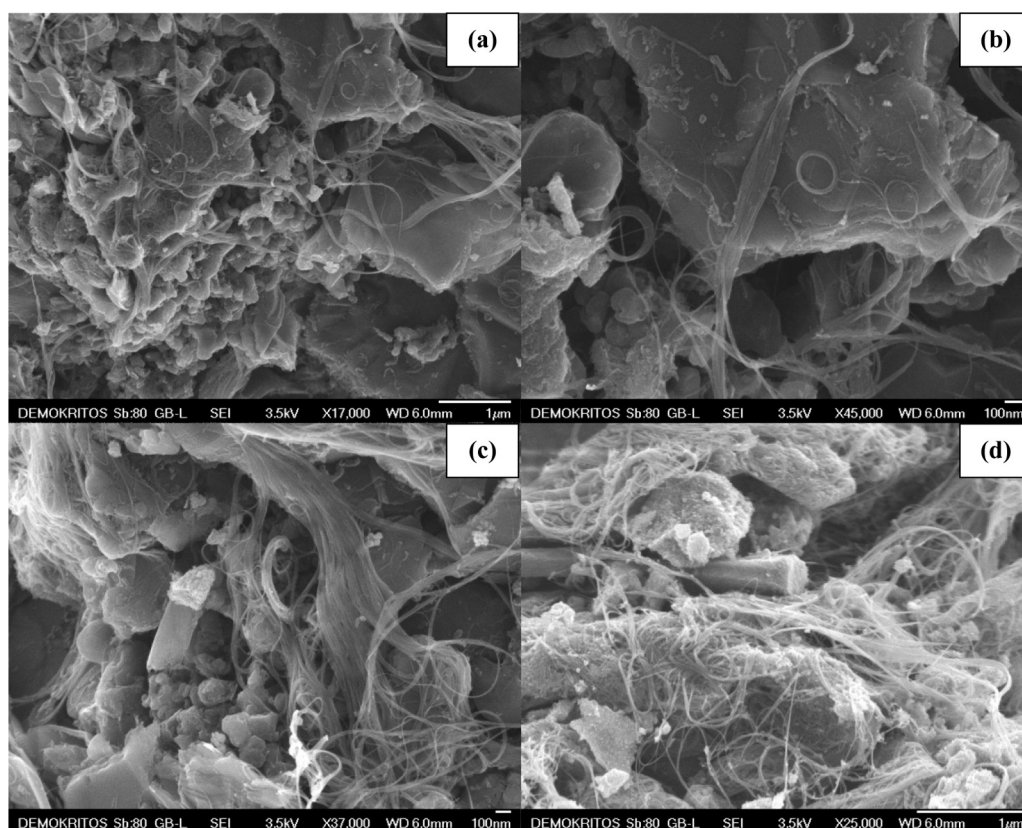


Fig. 6. SEM images of the hybrids prepared with SG and functionalized SWCNTs (SG/SNTf-20).

anatase mode that was hardly resolved for both the SA and P25/SNT composites, similar to that observed in  $\text{TiO}_2$ /SWCNT films [27]. Significantly larger frequency shifts of both the anatase  $E_{g(1)}$  SWCNTs Raman modes were observed only in the case of direct growth of  $\text{TiO}_2$  on SWCNT buckypaper by electrochemical deposition [29], which could greatly enhance the interfacial  $\text{TiO}_2$ –SWCNT interaction. On the other hand, the intriguing enhancement of the RBM intensity for the  $\text{TiO}_2$ /SNTf-20 implies an increase of the resonantly excited SWNTs upon mixing of the functionalized SWNTs with  $\text{TiO}_2$  [37]. Such an effect resembles the variation of the RBM intensity excitation profiles for bundled and highly dispersed SWCNTs, especially for the  $267\text{ cm}^{-1}$  mode arising from the  $\sim 0.9\text{ nm}$  (10.2) semiconducting SCWNTs [38] that dominates the Raman spectra at  $785\text{ nm}$ . The presence of an additional blue shift in the order of  $10\text{--}20\text{ meV}$  would be accordingly required to explain the RBM intensity enhancement for the  $\text{TiO}_2$ /SNTf-20 composites due to the textural modification of the SWCNT bundles upon mixing with the  $\text{TiO}_2$  probed by the  $\text{LN}_2$  porosimetry and SAXS analysis.

### 3.5. Raman spectroscopy on $\text{TiO}_2$ /MWCNT

Fig. 9 shows the Raman spectra of the SA/MNX and SA/MNXf composites compared with the corresponding ones of the pristine (MNX) and functionalized (MNXf) carbon nanotubes and the hydrated  $\text{SA-TiO}_2$  at  $514.5\text{ nm}$ . The anatase Raman modes were clearly observed for the SA/MNXf composites with small frequency shifts ( $\sim 1\text{ cm}^{-1}$  for the  $E_{g(1)}$  mode), indicative of weak  $\text{TiO}_2$ –MWCNTs electronic coupling, similar to their  $\text{TiO}_2$ /SNT analogues.

MWCNTs were detected in the composite materials by their characteristic Raman bands, i.e. the tangential G band at  $1585\text{ cm}^{-1}$ , the defect-induced D band at  $1354\text{ cm}^{-1}$  and its overtone  $G'$  band at  $2706\text{ cm}^{-1}$ , as can be seen in Fig. 10b. Moreover, two additional

defect-induced modes of lower intensity, the  $D'$  band appearing as a shoulder to the G band at  $\sim 1622\text{ cm}^{-1}$  arising from a similar double resonance process as the D-band [34], and the relatively broad  $D+D'$  combination mode at  $\sim 2950\text{ cm}^{-1}$  [39] were observed for the SA- $\text{TiO}_2$ /MWCNT composites (Fig. 10b).

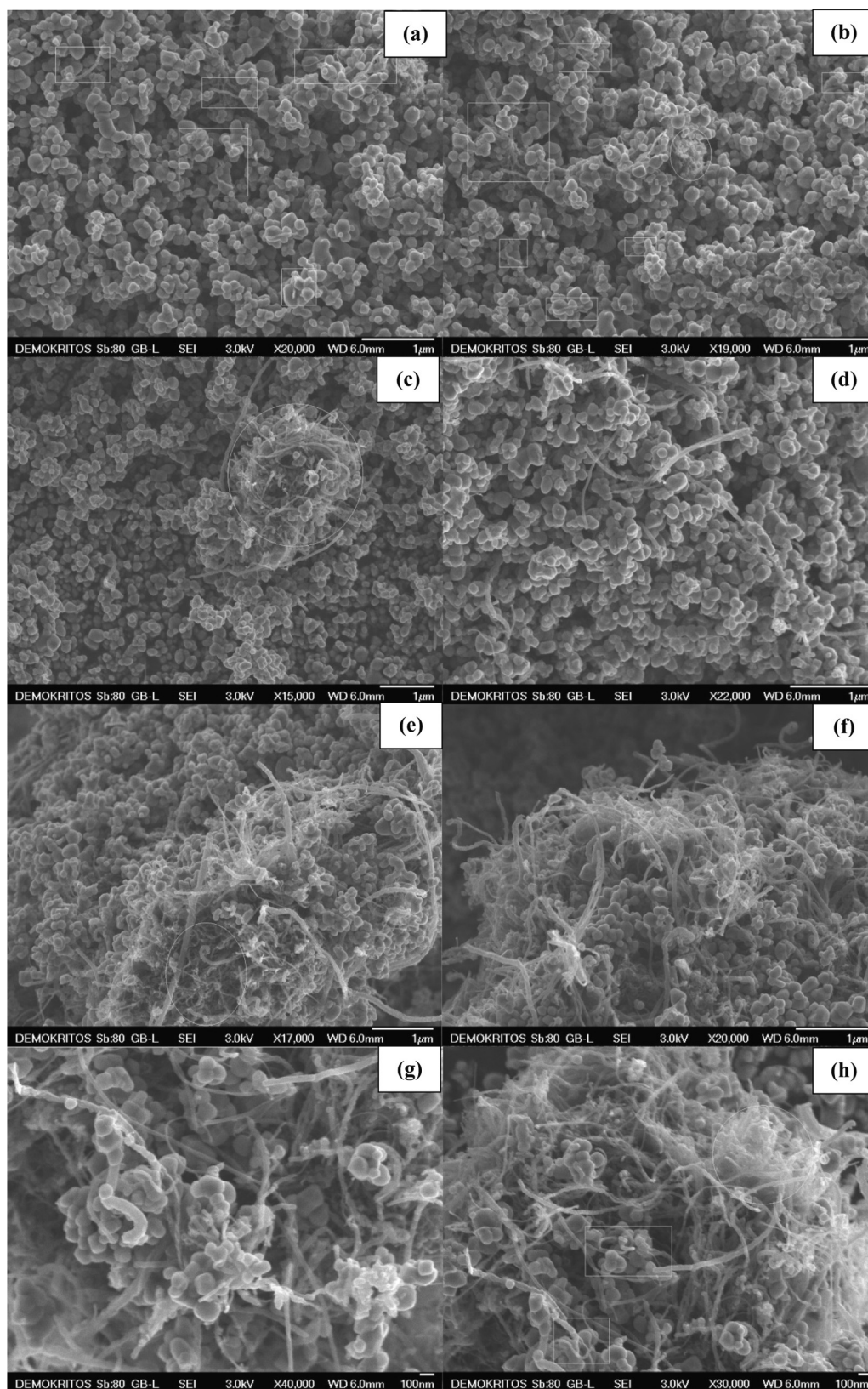
Spectral analysis of these modes by multi-peak fitting revealed minor frequency shifts ( $\sim 1\text{ cm}^{-1}$ ) for the SA/MNX composites compared with the pristine (MNX) and functionalized (MNXf). On the contrary, the relative intensity ratios  $I_D/I_G$ ,  $I_{D'}/I_G$  and  $I_{D+D'}/I_G$ , obtained from the integrated intensities of the D,  $D'$ ,  $D+D'$  and G bands, were found to increase for the MNXf and even more drastically for the composite materials, as summarized in Table 4. This variation was further corroborated by the corresponding Raman spectra at  $785\text{ nm}$  excitation (not shown).

While the increase of the intensity ratios for the defect-induced modes is well accounted by the formation of oxygen groups on the surface of MNXf upon nitric acid oxidation [35], a further increase of the defect density can be concluded for the SA/MNXf composites [40,41]. Furthermore, the enhancement of the defect induced modes for the SA/MNXf composites. This was accompanied by the simultaneous decrease of the  $G'$  band relative intensity monitored through the  $I_{G'}/I_G$  ratio (Table 4). As the  $G'$  band is very sensitive to

Table 4

Integrated intensity ratios of the D,  $D'$ ,  $D+D'$  and  $G'$  bands for the SA- $\text{TiO}_2$ /MWCNT composites compared with the pristine and functionalized MWCNTs at  $514.5\text{ nm}$ .

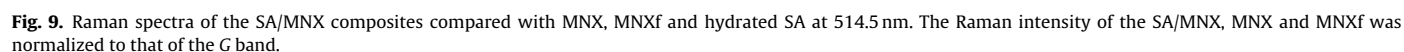
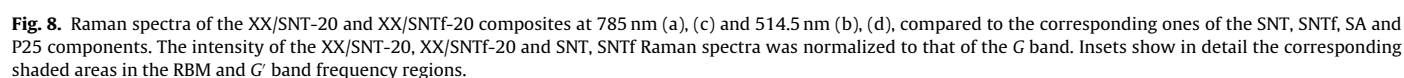
Sample	$I_D/I_G$	$I_{D'}/I_G$	$I_{D+D'}/I_G$	$I_{G'}/I_G$
MNX	0.55	0.07	0.17	2.18
MNXf	0.84	0.11	0.33	2.01
SA/MNXf-20	1.01	0.15	0.46	1.67
SA/MNXf-10	1.01	0.17	0.39	1.66
SA/MNXf-5	0.98	0.20	0.60	1.70
SA/MNP-10	0.68	0.09	0.24	1.71



**Fig. 7.** SEM images of the hybrids prepared with SA and functionalized MWCNTs. (a–c) SA/MNXf-5, (d–f) SA/MNXf-10, (g and h) SA/MNXf-20.

the stacking order of the graphitic walls and the in-plane coherence length of MWCNTs [34], the observed decrease of  $I_G/I_G$  implies a degradation of the structural conformation of MWCNTs in the composite materials. This effect can be associated with the distortion

of the outermost shells of MWCNTs upon their entanglement and grafting with the large SA-TiO<sub>2</sub> particles, which effectively deteriorate the graphitic ordering of the MWCNTs and thus decrease the  $G'$  band intensity. Overall, the observed variation of the relative





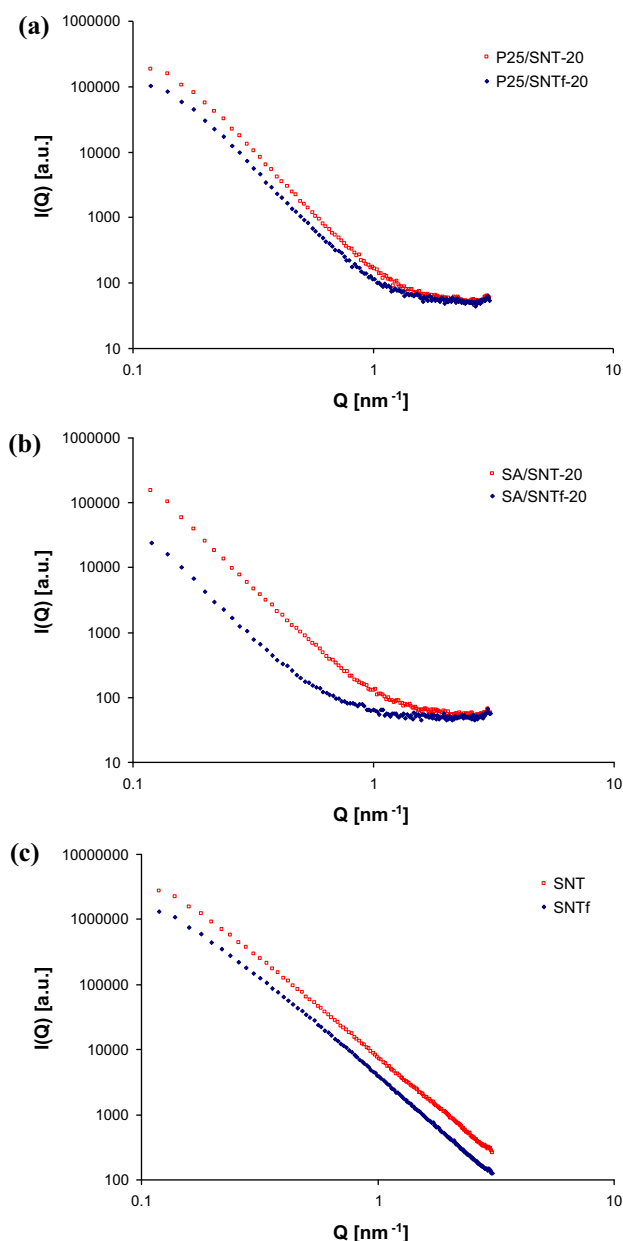


**Fig. 10.** SAXS curves of (a) the hybrids prepared with P25 and SWCNTs, (b) the hybrids prepared with SA and SWCNTs and (c) the pristine SWCNTs and functionalized SWCNTs. Note that in case of (c) the curves are almost identical and they have been shifted by a factor of 2 for clarity.

intensities of the MWCNTs Raman bands verifies that wet mixing of  $\text{TiO}_2$  particles with MWCNTs, similar to the  $\text{TiO}_2$ /SWCNT composites, resembles the effect of defect creation on the MWCNT surface. On the other hand, no evidence for the presence strong interfacial charge transfer between the two constituent phases,  $\text{TiO}_2$  and MWCNTs, could be obtained based on the absence of any significant Raman shifts.

### 3.6. SAXS measurements

The SAXS curves of all samples do not exhibit Bragg reflections excluding any close packing of nanotubes and/or  $\text{TiO}_2$  particles (Fig. 10). Further, the SAXS profiles decay following a power law ( $I(Q) \propto Q^{-a}$ ). According to the theory, when  $3 < a < 4$  the data are interpreted as scattering from surfaces. Bale and Schmidt [42] derived  $a = 6 - D_s$  for a rough interface with a surface fractal

**Table 5**

Surface fractal dimension,  $D_s$  of SWCNTs and  $\text{TiO}_2$ /SWCNT composites obtained from the SAXS curves.

Sample	$D_s$
SNT	3.0
SNTf	2.9
P25/SNT-20	2.3
P25/SNTf-20	2.4
SA/SNT-20	2.6
SA/SNTf-20	2.6

dimension  $2 < D_s < 3$ . Apparently for a smooth surface  $a = 4$  and  $D_s = 2$  (the Porod's law [43]) has been predicted. The scattering curves of SNT and SNTf are almost identical with values of  $D_s$  3.0 and 2.9 respectively (Fig. 10c, Table 5). This result is reasonable as neither for pristine nor for functionalized SWCNTs a smooth surface is expected because pristine SWCNTs have numerous carbonaceous impurities like carbon black, defects on their carbon networks and twists which lead to a rough surface [44].

Fig. 10a and b shows the SAXS profiles of hybrids prepared with  $\text{TiO}_2$  and SWCNTs. An interesting finding is that the hybrids prepared with P25 have values of  $D_s$  closer to 2 compared to those prepared with SA (Table 5). This could be attributed to the fact that the particle size of P25 is comparable with this of the SWCNT bundles resulting in a smoother  $\text{TiO}_2$ /SWCNT bundle interface. One can also observe that the patterns of all hybrids exhibit a flat regime in the high  $Q$  region. The presence of the plateau is indicative for the existence of micropores [45–47]. However, in the case of the sample consisting of SA and SNTf the plateau is extended to a lower  $Q$  region implying a shift of the size distribution of micropores towards larger values.

### 3.7. Photocatalytic experiments

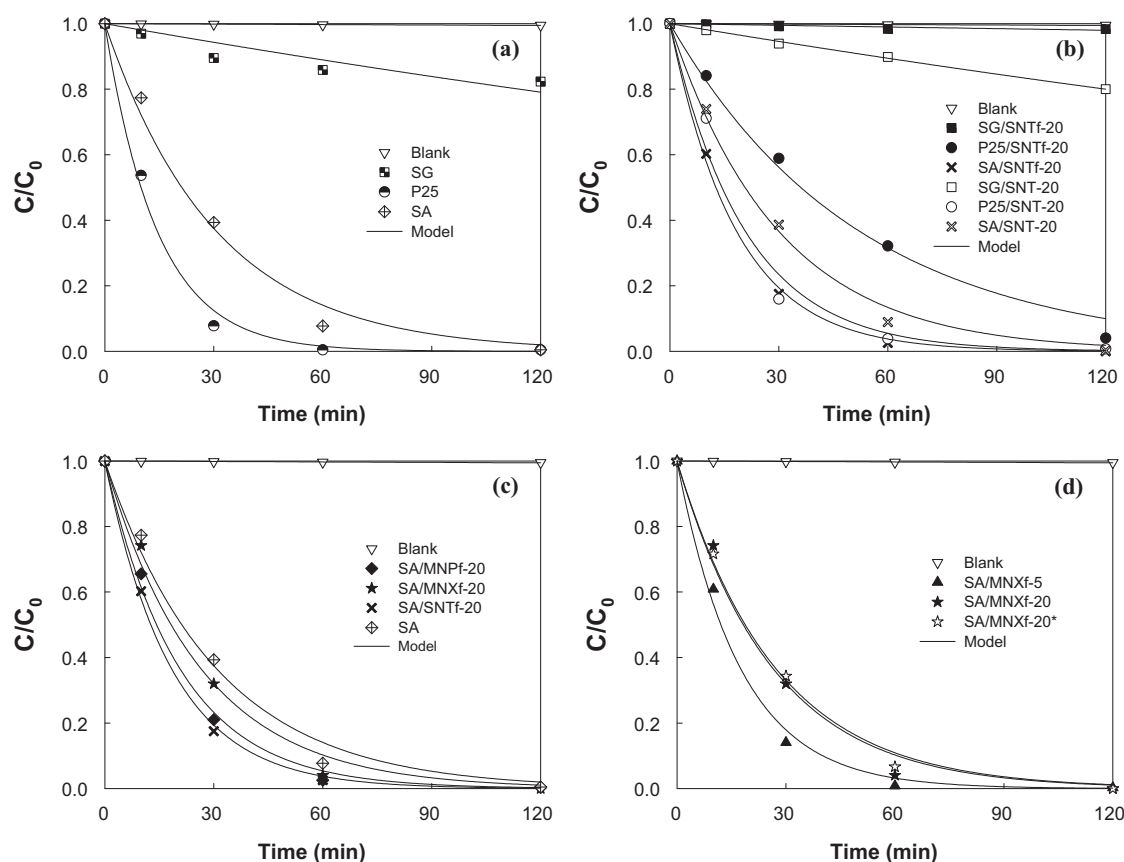
#### 3.7.1. Photocatalytic activity of bare $\text{TiO}_2$ materials

Fig. 11a shows the caffeine concentration evolution in the photocatalytic experiments performed with bare  $\text{TiO}_2$  materials together with the results obtained for the non-catalytic run (photolysis – blank). Caffeine is very stable under non-catalytic conditions while all tested catalysts increased the caffeine degradation rate. The experiments revealed that the photocatalytic oxidation of caffeine could be ascribed to a pseudo-first order kinetic model, as described by the following equation:

$$C = C_0 e^{-kt} \quad (3)$$

where  $C$  corresponds to pollutant concentration,  $k$  is the pseudo-first order kinetic constant,  $t$  is the reaction time and  $C_0$  is the pollutant concentration for  $t = 0$ . The  $k$  values were obtained by non-linear regression, fitting Eq. (3) to the normalized caffeine concentration evolution ( $C/C_0$ ). The used Marquardt–Levenberg algorithm seeks the values of the parameters that minimize the sum of the squared differences between observed and predicted values of the dependent variable (the tolerance was set at  $1 \times 10^{-10}$ ). The standard error of each estimated  $k$  parameter and the respective regression coefficient of the model ( $r^2$ ) are shown in Table 6 and indicate in general good fitting of the model to the experimental data.

The respective pseudo-first order rate constants ( $k$ ) are shown in Table 6, namely  $k = 1.9 \times 10^{-3}$ ,  $33 \times 10^{-3}$  and  $69 \times 10^{-3} \text{ min}^{-1}$  for SG, SA and P25, respectively, and only  $0.05 \times 10^{-3} \text{ min}^{-1}$  for the pure photolysis. The order of photocatalytic activity was exactly the same that was found in our previous publication [23] employing those bare  $\text{TiO}_2$  materials with a UV–vis medium pressure mercury vapor lamp and using other photocatalytic reactor and experimental conditions (namely:  $k = 4.9 \times 10^{-3}$ ,  $26 \times 10^{-3}$  and  $123 \times 10^{-3} \text{ min}^{-1}$  for SG, SA and P25, respectively,



**Fig. 11.** Photolytic (blank) and photocatalytic degradation of caffeine over (a) bare  $\text{TiO}_2$  materials, (b) composites prepared with functionalized SWCNTs (XX/SNTf-20) and non-functionalized SWCNTs (XX/SNT-20), (c) SA-based composites prepared with different functionalized CNTs, namely MWCNTs (SA/MNPF-20 and SA/MNXf-20) and SWCNTs (SA/SNTf-20), (d) SA-based composites prepared with different MWCNT:TiO<sub>2</sub> ratios (SA/MNXf-20\* refers to the composite prepared with manual mixing). Curves represent the fitting of the pseudo-first order equation to the experimental data.

and  $0.36 \times 10^{-3} \text{ min}^{-1}$  for photolysis). Therefore, for the photocatalysts consisting of anatase crystalline form, SA having the larger average anatase crystallite sizes of  $\text{TiO}_2$  (50–100 nm) performs clearly better than SG (9 nm), while P25 consisting of both anatase and rutile crystalline phases is the most effective bare  $\text{TiO}_2$  material for caffeine photocatalytic degradation.

### 3.7.2. Photocatalytic activity of $\text{TiO}_2/\text{CNT}$ composites

The results obtained for the photocatalytic degradation of caffeine using composites prepared with non-functionalized

(XX/SNT-20) and functionalized (XX/SNTf-20) single-wall CNTs are shown in Fig. 11b. These results show that the oxygenated groups introduced on the carbon nanotubes play an important role in the catalytic activity of the composites prepared with SA. The caffeine conversion increased from 61% (with non-functionalized SWCNTs) to 81% (with functionalized SWCNTs) in 30 min, and the respective pseudo-first order rate constants from  $34 \times 10^{-3}$  to  $55 \times 10^{-3} \text{ min}^{-1}$  (Table 6), caffeine being completely degraded in 120 min. The same trend was observed in our previous publication with  $\text{TiO}_2/\text{CNT}$  composites prepared with the MNP carbon nanotubes, namely the pseudo-first order rate constants increased from  $17 \times 10^{-3}$ , when using the pristine MWCNTs, to  $63 \times 10^{-3} \text{ min}^{-1}$ , when using functionalized MWCNTs, both with a mass ratio of 10 [23]. Therefore, it is important to refer that the photocatalytic activity of SA-based composites always increased when functionalized CNTs were used instead of non-functionalized CNTs, becoming clear the benefit of functionalized CNTs on the photocatalytic activity of SA-based materials, regardless the nature (SWCNTs or MWCNTs) and the mass ratio (10 or 20) of CNTs.

In fact, the nitric acid treatment introduces oxygenated groups in the poor surface of the CNTs, as shown in TPD spectra obtained for non-functionalized and functionalized SWCNTs (not shown). By using a deconvolution methodology described elsewhere for TPD spectra [48], mainly carboxylic acids (evolved as  $\text{CO}_2$ ) and phenols (released as CO) were found in the surface of the functionalized SWCNTs. These surface groups are thought to promote the dispersion of  $\text{TiO}_2$  particles and also expected to contribute for the formation of Ti–O–C bonds, driven by esterification reactions between the carboxylic acid groups of the carbon nanotubes and the hydroxy groups of  $\text{TiO}_2$  [49]. Besides the high number of surface oxygenated

**Table 6**

Pseudo-first order kinetic rate constants ( $k$ ) and respective standard errors for the photolytic and photocatalytic degradation of caffeine using different catalysts. The regression coefficients ( $r^2$ ) are also presented.

Sample	$k$ ( $10^{-3} \text{ min}^{-1}$ )	$r^2$
Blank	$0.05 \pm 0.01$	0.89
SG	$1.9 \pm 0.5$	0.8
SG/SNT-20	$1.9 \pm 0.1$	0.997
SG/SNTf-20	$0.2 \pm 0.1$	0.8
P25	$69 \pm 6$	0.995
P25/SNT-20	$48 \pm 8$	0.98
P25/SNTf-20	$19 \pm 2$	0.993
SA	$33 \pm 4$	0.99
SA/SNT-20	$34 \pm 2$	0.996
SA/SNTf-20	$55 \pm 3$	0.999
SA/MNXf-5	$57 \pm 5$	0.995
SA/MNXf-20	$38 \pm 4$	0.991
SA/MNXf-20 <sup>a</sup>	$37 \pm 3$	0.996
SA/MNPF-20	$49 \pm 4$	0.996

<sup>a</sup> Prepared by manual mixing.

groups, a unique characteristic of the SA/SNTf-20 sample was that its pore structure was dominated by the existence of micropores with larger size. As revealed by SAXS analysis, the sample SA/SNTf-20 was the only one for which the decrease of the ultramicropore volume led to the formation of wider micropores, a characteristic that could not be distinguished via the LN<sub>2</sub> experiments. In this regard we can state that the high rate and enhanced capacity for caffeine degradation exhibited from this specific sample was the outcome of both photocatalytic efficiency and adsorption. The reason behind this behaviour is that wider micropores may be accessible for caffeine to diffuse, being adsorbed, something that could not happen for the rest of the prepared composites.

Indeed, the marked increase of the photocatalytic activity observed when functionalized SWCNTs are used in the preparation of the composites with SA was not observed for P25- and SG-based composites. The pseudo-first order rate constants decreased from  $48 \times 10^{-3}$  to  $19 \times 10^{-3} \text{ min}^{-1}$  for P25/SNT-20 and P25/SNTf-20, and from  $1.9 \times 10^{-3}$  to  $0.2 \times 10^{-3} \text{ min}^{-1}$  for SG/SNT-20 and SG/SNTf-20, respectively (Table 6, Fig. 11b).

Interestingly, the photocatalytic activity observed for most of the tested composites is directly related with the previous determined decrease of the SWCNTs microporosity, which expresses better mixing quality (disentanglement of the SWCNTs bundles or plugging of the SWCNTs bore space), i.e. from Tables 2 and 6: P25/SNT-20 ( $48 \times 10^{-3} \text{ min}^{-1}$ )  $\gg$  SA/SNT-20 ( $34 \times 10^{-3} \text{ min}^{-1}$ )  $\approx$  SA/SNTf-20 ( $55 \times 10^{-3} \text{ min}^{-1}$ )  $\gg$  P25/SNTf-20 ( $19 \times 10^{-3} \text{ min}^{-1}$ )  $\approx$  SG/SNT-20 ( $1.9 \times 10^{-3} \text{ min}^{-1}$ )  $>$  SG/SNTf-20 ( $0.2 \times 10^{-3} \text{ min}^{-1}$ ), the numbers in brackets corresponding to the pseudo-first order rate constants.

Therefore, the only material that deviates from this trend is the SA/SNTf-20 composite, which is that presenting the higher photocatalytic activity. This means that the resulting wider micropores dictated in a large extent the respective photocatalytic activity but, besides, other properties should have influence on the photocatalytic properties of the TiO<sub>2</sub>/CNT composites.

Obviously, the nature of the TiO<sub>2</sub> phase is important (as verified with the bare TiO<sub>2</sub> materials in Fig. 11a), however, when comparing composites consisting of the same TiO<sub>2</sub> phase – but having very different microporosity (i.e. composites based on P25 as well as those based on SG, Table 2) – the correlation between the microporosity and the photocatalytic activity for these materials is maintained, namely P25/SNT-20 ( $48 \times 10^{-3} \text{ min}^{-1}$ )  $>$  P25/SNTf-20 ( $19 \times 10^{-3} \text{ min}^{-1}$ ) and SG/SNT-20 ( $1.9 \times 10^{-3} \text{ min}^{-1}$ )  $>$  SG/SNTf-20 ( $0.2 \times 10^{-3} \text{ min}^{-1}$ ). However, in the particular case of SA-based composites (SA/SNTf-20 and SA/SNT-20), the deviations on SWCNTs microporosity are very similar (Table 2) and it seems that for this reason the well-known positive effect of the functionalization of CNTs on the photocatalytic activity was only distinguished for SA-based composites ( $k = 34 \times 10^{-3}$  and  $55 \times 10^{-3} \text{ min}^{-1}$  for SA/SNT-20 and SA/SNTf-20, respectively). It can be concluded then that for materials with the same deviation of microporosity (e.g. similar mixing quality), as is the case of SA/SNT-20 and SA/SNTf-20, functional groups on the CNTs can have a benefic effect on the photocatalytic efficiency.

Fig. 11c shows the results obtained with the SA/MNXf-20 composite and, for comparison, results with SWCNTs (SA/SNTf-20), other MWCNTs (SA/MNPF-20) and bare SA are also included. The SA/MNXf-20 composite ( $k = 38 \times 10^{-3} \text{ min}^{-1}$ ) has a significant lower activity than the SA/SNTf-20 composite ( $k = 55 \times 10^{-3} \text{ min}^{-1}$ ), or even than SA/MNPF-20 ( $k = 49 \times 10^{-3} \text{ min}^{-1}$ ). In addition, as expected, the SA/MNPF-20 composite was more active than bare SA ( $k = 33 \times 10^{-3} \text{ min}^{-1}$ ), as already demonstrated in our previous work under other conditions [23].

An experiment was additionally performed with the material prepared with a lower amount of MWCNTs, i.e. SA/MNXf-5

(Fig. 11d). It was verified that a lower mass ratio of MWCNTs leads to a higher efficiency, being the pseudo-first order rate constants  $57 \times 10^{-3}$  and  $38 \times 10^{-3} \text{ min}^{-1}$  for SA/MNXf-5 and SA/MNXf-20, respectively (Table 6). Therefore, once again, it seems that the homogeneity of the composite has a predominant influence on the respective photocatalytic activity, since SA/MNXf-5 has a much larger deviation on the microporosity than SA/MNXf-20 (Table 2), and also presents a higher photocatalytic activity. Comparable activities were obtained with SA/MNXf-5 ( $57 \pm 5 \times 10^{-3} \text{ min}^{-1}$ ) and with SA/SNTf-20 ( $k = 55 \pm 3 \times 10^{-3} \text{ min}^{-1}$ ).

The enhancement of the activity and the respective cost of the material should be balanced when selecting the precursors of a photocatalyst. Therefore, MWCNTs seems to be more interesting for actual applications due to the recent advances on their large-scale production and, as consequence, their lower cost in comparison to SWCNTs.

In order to verify the possible influence of the hydration/dehydration method on the photocatalytic activity, other additional experiment was performed with SA/MNXf-20 but in this case prepared by manual mixing of SA and MNXf (referred as SA/MNXf-20\* in Fig. 11d and Table 6). The obtained photocatalytic degradation of caffeine with SA/MNXf-20\* ( $k = 37 \times 10^{-3} \text{ min}^{-1}$  for SA/MNXf-20\* and  $38 \times 10^{-3} \text{ min}^{-1}$  for SA/MNXf-20) confirms that the hydration/dehydration method employed has the same effect than the manual mixing on the photocatalytic properties of these composites.

Overall, under the conditions tested in the present fundamental study, the benchmark photocatalyst (P25) was the most active material tested. However, the separation of nanomaterials from the treated water requires critical separation steps that should be considered for the materials technological implementation, being the major concerns the effects on the public health and environment. In our previous work [23] was demonstrated that SA/CNTf-20 films are promising for technological applications, as alternative to powder suspensions, presenting significantly higher activity than films prepared with P25 (not only to degrade caffeine but also diphenhydramine pharmaceutical) and, therefore, further studies regarding catalyst activity and stability in continuous operation are still needed, being the present study a step forward in the understanding of the enhancement of the photocatalytic activity when CNTs are combined with the SA material.

#### 4. Conclusions

Results show that the simple hydration/dehydration method is not adequate to generate TiO<sub>2</sub>/CNT composites with intimate contact between the two phases, in a way that could trigger synergetic effects via interfacial charge transfer. Following that conclusion, a new LN<sub>2</sub> methodology to assess the photocatalytic degradation efficiency as function of the mixing quality in the synthesized composites is proposed. The results on caffeine degradation showed a very good correlation of the elucidated mixing quality with the photocatalytic efficiency.

An unexpected finding was that the functionalization of the SWCNTs does not facilitate the mixing between the constituent phases of the composite. Thus all composites based on functionalized CNTs had lower photocatalytic efficiencies than that of the composites based on pristine CNTs. This was attributed to the generation of self-standing bundles where the nanotubes remain tangled through stronger van der Waals forces. Though the bundles were better dispersed in the water solution during hydration, the nanotubes in each bundle were not disentangled to decorate the surface of the nanoparticles.

An exception to this rule observed for one of the samples was mainly attributed to the generation of wide micropores a feature

revealed by SAXS experiments. With regard to this, it is believed that the better caffeine removal efficiency of this sample compared to that prepared with pristine CNTs was due to an additional contribution of caffeine adsorption in this specific class of wider micropores.

## Acknowledgements

Financial support for this work was provided by projects PTDC/EQU-EQU/100554/2008, PTDC/AAC-AMB/122312/2010 and PEst-C/eqb/LA0020/2011, financed by FEDER through COMPETE and by FCT – Fundação para a Ciência e a Tecnologia. The authors also acknowledge financial support by the European Commission (Clean Water – Grant Agreement n° 227017). RRNM acknowledges financial support from SFRH/BD/65425/2009.

## References

- [1] W.C. Oh, F.J. Zhang, M.L. Chen, *Asian J. Chem.* 22 (2010) 2231–2243.
- [2] T.-T. Duong, Q.-D. Nguyen, S.-K. Hong, D. Kim, S.-G. Yoon, T.-H. Pham, *Adv. Mater.* 23 (2011) 5557–5562.
- [3] M.J. Sampaio, C.G. Silva, R.R.N. Marques, A.M.T. Silva, J.L. Faria, *Catal. Today* 161 (2011) 91–96.
- [4] T.A. Saleh, V.K. Gupta, *J. Colloid Interface Sci.* 371 (2012) 101–106.
- [5] T.H.T. Vu, T.T.T. Nguyen, P.H.T. Nguyen, M.H. Do, H.T. Au, T.B. Nguyen, D.L. Nguyen, *J.S. Park, Mater. Res. Bull.* 47 (2012) 308–314.
- [6] C.G. Silva, J.L. Faria, *Appl. Catal. B: Environ.* 101 (2010) 81–89.
- [7] B. Gao, G.Z. Chen, G. Li Puma, *Appl. Catal. B: Environ.* 89 (2009) 503–509.
- [8] W. Zhou, K. Pan, Y. Qu, F. Sun, C. Tian, Z. Ren, G. Tian, H. Fu, *Chemosphere* 81 (2010) 555–561.
- [9] N. Bouazza, M. Ouzzine, M.A. Lillo-Ródenas, D. Eder, A. Linares-Solano, *Appl. Catal. B: Environ.* 92 (2009) 377–383.
- [10] Z. Li, B. Gao, G.Z. Chen, R. Mokaya, S. Sotiropoulos, G. Li Puma, *Appl. Catal. B: Environ.* 110 (2011) 50–57.
- [11] K.H. Ji, D.M. Jang, Y.J. Cho, Y. Myung, H.S. Kim, Y. Kim, J. Park, *J. Phys. Chem. C* 113 (2009) 19966–19972.
- [12] G. An, W. Ma, Z. Sun, Z. Liu, B. Han, S. Miao, Z. Miao, K. Ding, *Carbon* 45 (2007) 1795–1801.
- [13] T. Tsubota, A. Ono, N. Murakami, T. Ohno, *Appl. Catal. B: Environ.* 91 (2009) 533–538.
- [14] Y. Yao, G. Li, S. Ciston, R.M. Lueptow, K.A. Gray, *Environ. Sci. Technol.* 42 (2008) 4952–4957.
- [15] W. Wang, P. Serp, P. Kalck, J.L. Faria, *J. Mol. Catal. A: Chem.* 235 (2005) 194–199.
- [16] B.K. Vijayan, N.M. Dimitrijevic, D. Finkelstein-Shapiro, J. Wu, K.A. Gray, *ACS Catal.* 2 (2011) 223–229.
- [17] J. Sun, M. Iwasa, L. Gao, Q. Zhang, *Carbon* 42 (2004) 895–899.
- [18] C.Y. Yen, Y.F. Lin, C.H. Hung, Y.H. Tseng, C.C. Ma, M.C. Chang, H. Shao, *Nanotechnology* 19 (2008) 045604.
- [19] H. Wang, H.-L. Wang, W.-F. Jiang, Z.-Q. Li, *Water Res.* 43 (2009) 204–210.
- [20] Y. Gao, H. Liu, M. Ma, *React. Kinet. Catal. Lett.* 90 (2007) 11–18.
- [21] C. Martínez, M. Canle, L.M.I. Fernández, J.A. Santaballa, J. Faria, *Appl. Catal. B: Environ.* 102 (2011) 563–571.
- [22] K. Woan, G. Pyrgiotakis, W. Sigmund, *Adv. Mater.* 21 (2009) 2233–2239.
- [23] R.R.N. Marques, M.J. Sampaio, P.M. Carrapiço, C.G. Silva, S. Morales-Torres, G. Dražić, J.L. Faria, A.M.T. Silva, *Catal. Today* 209 (2013) 108–115.
- [24] V. Likodimos, T. Stergiopoulos, P. Falaras, J. Kunze, P. Schmuki, *J. Phys. Chem. C* 112 (2008) 12687–12696.
- [25] A.I. Kontos, A.G. Kontos, D.S. Tsoukleris, M.-C. Bernard, N. Spyrellis, P. Falaras, *J. Mater. Process. Technol.* 196 (2008) 243–248.
- [26] M.S. Dresselhaus, G. Dresselhaus, R. Saito, A. Jorio, *Phys. Rep.* 409 (2005) 47–99.
- [27] K.-H. Jung, S.-R. Jang, R. Vittal, V.D. Kim, K.-J. Kim, *Bull. Korean Chem. Soc.* 24 (2003) 1501–1504.
- [28] Y. Yu, J.C. Yu, C.-Y. Chan, Y.-K. Che, J.-C. Zhao, L. Ding, W.-K. Ge, P.-K. Wong, *Appl. Catal. B: Environ.* 61 (2005) 1–11.
- [29] M. Kalbac, O. Frank, L. Kavan, M. Zúkalová, J. Procházka, M. Klementová, L. Dunsch, *J. Electrochem. Soc.* 154 (8) (2007) K19–K24.
- [30] S.H. Sharif Zein, A.R. Boccaccini, *Ind. Eng. Chem. Res.* 47 (2008) 6598–6606.
- [31] A.M.O. Zavallos-Márquez, M.J.S.P. Brasil, F. Iikawa, A. Abbaspourrad, C. Verissimo, S.A. Moshkalev, O.L. Alves, *J. Appl. Phys.* 108 (2010) 083501.
- [32] F. Inoue, R.A. Ando, P. Corio, *J. Raman Spectrosc.* 42 (2011) 1379–1383.
- [33] J. Yu, T. Ma, S. Liu, *Phys. Chem. Chem. Phys.* 13 (2011) 3491–3501.
- [34] M.A. Pimenta, G. Dresselhaus, M.S. Dresselhaus, L.G. Cancado, A. Jorio, R. Saito, *Phys. Chem. Chem. Phys.* 9 (2007) 1276–1290.
- [35] G.E. Romanos, V. Likodimos, R.R.N. Marques, T.A. Steriotis, S.K. Papageorgiou, J.L. Faria, J.L. Figueiredo, A.n.M.T. Silva, P. Falaras, *J. Phys. Chem. C* 115 (2011) 8534–8546.
- [36] L. Kavan, L. Dunsch, *ChemPhysChem* 8 (2007) 974–998.
- [37] P.T. Araujo, S.K. Doorn, S. Kilina, S. Tretiak, E. Einarsson, S. Maruyama, H. Chacham, M.A. Pimenta, A. Jorio, *Phys. Rev. Lett.* 98 (2007) 067401.
- [38] M.J. O'Connell, S. Sivaram, S.K. Doorn, *Phys. Rev. B* 69 (2004) 235415.
- [39] C. Fantini, M.A. Pimenta, M.S. Strano, *J. Phys. Chem. C* 112 (2008) 13150–13155.
- [40] Y. Yu, J.C. Yu, J.-G. Yu, Y.-C. Kwok, Y.-K. Che, J.-C. Zhao, L. Ding, W.-K. Ge, P.-K. Wong, *Appl. Catal. A: Gen.* 289 (2005) 186–196.
- [41] S. Santangelo, G. Messina, G. Faggio, A. Donato, L. De Luca, N. Donato, A. Bonavita, G. Neri, *J. Solid State Chem.* 183 (2010) 2451–2455.
- [42] H.D. Bale, P.W. Schmidt, *Phys. Rev. Lett.* 53 (1984) 596–599.
- [43] G. Porod, in: O. Glatter, O. Kratky (Eds.), *Small Angle X-ray Scattering*, Academic Press, London, 1982, pp. 17–51.
- [44] A.A. Golosova, J. Adelsberger, A. Sepe, M.A. Niedermeier, P. Lindner, S.S. Funari, R. Jordan, C.M. Papadakis, *J. Phys. Chem. C* 116 (2012) 15765–15774.
- [45] A.C. Mitropoulos, K.L. Stefanopoulos, N.K. Kanellopoulos, *Microporous Mesoporous Mater.* 24 (1998) 29–39.
- [46] J.M. Calo, P.J. Hall, *Carbon* 42 (2004) 1299–1304.
- [47] E.P. Favvas, K.L. Stefanopoulos, S.K. Papageorgiou, A.C. Mitropoulos, *Adsorption* 19 (2013) 225–233.
- [48] J.L. Figueiredo, M.F.R. Pereira, M.M.A. Freitas, J.J.M. Órfão, *Carbon* 37 (1999) 1379–1389.
- [49] Q. Wang, D. Yang, D. Chen, Y. Wang, Z. Jiang, *J. Nanopart. Res.* 9 (2007) 1087–1096.